# TECHNICAL UNIVERSITY OF CARTAGENA

## DEPARTMENT OF INFORMATION AND COMMUNICATION TECHNOLOGIES

Master Thesis

# Reconfigurable Plasmonic Filters and Spatial Dispersion Effects in Graphene Technology for Terahertz Applications.

etsit
escuela técnica superior de
ingeniería de telecomunicación

AUTHOR: Diego Correas Serrano

SUPVERVISOR: Alejandro Álvarez Melcón

CO-SUPERVISOR: Juan Sebastián Gómez Díaz

Cartagena, June 2015

| Author | Diego Correas Serrano |
|---|---|
| Author's email | diego.correas.serrano@gmail.com |
| Supervisor | Alejandro Álvarez Melcón |
| Supervisor's email | alejandro.alvarez@upct.es |
| Supervisor | Juan Sebastián Gómez Díaz |
| Title | Reconfigurable Plasmonic Filters and Spatial Dispersion Effects in Graphene Technology for Terahertz Applications. |
| Título | Filtros Plasmónicos Reconfigurables y Fenómenos de Dispersión Espacial en Tecnología de Grafeno en la Banda de Terahercios. |

**Abstract**

The exceptional electrooptical, thermal, and mechanical properties of graphene has motivated an enormous interest from the scientific community in a wide variety of fields in recent years. In particular, the capability of mono- and multi-layer graphene to support highly confined reconfigurable surface plasmon polaritons in the terahertz (THz) and infrared regime has motivated an explosive growth of graphene plasmonics, a discipline which is paving the way towards fully integrated THz transceivers and sensing systems. In this project, we first present the novel design and analysis of planar reconfigurable THz filters hosted in graphene nanoribbons, which are efficiently designed taking advantage of the quasi-static nature of graphene surface plasmon polaritons (SPPs) in nanostructures and graphene's field effect. The proposed filters are highly miniaturized and present reconfiguration capabilities not possible with other technologies in the THz band. Spatial dispersion in graphene sheets is then reviewed. This effect is closely related to the quantum capacitance of graphene and strongly affects surface wave propagation under certain circumstances. This phenomenon is studied in the THz and near infrared frequency bands, and accurate equivalent circuits that provide deep physical insight and simplify design tasks are developed. The practical implications of spatial dispersion regarding THz graphene-based plasmonic devices like the filters mentioned above are discussed.

**Resumen**

Las excepcionales propiedades térmicas, mecánicas y electro-ópticas del grafeno han atraído un enorme interés de las comunidades científicas de diversas áreas en los últimos años. La capacidad del grafeno de soportar la excitación y propagación de plasmones de superficie en la bandas de terahercios (THz) e infrarrojos han motivado un crecimiento explosivo del estado del arte en cienca y tecnología de plasmones en estas bandas de frecuencias, una disciplina que podría ser crucial para el futuro desarrollo de sistemas integrados y altamente miniaturizados de comunicación, detección y sensores. En este proyecto, se presenta en primer lugar la síntesis y análisis de filtros planares reconfigurables en la banda de THz mediante control electrostático de plasmones en tiras de grafeno. Se ha desarrollado una técnica de diseño eficiente, explotando la naturaleza cuasi-estática de este tipo de ondas electromagnéticas en tiras de ancho mucho menor que la longitud de onda. Se ilustra el rendimiento de estos filtros con múltiples ejemplos, demostrando capacidades de reconfiguración que no son posibles con otras tecnologías.

Posteriormente se estudia de forma analítica el fenómeno de dispersión espacial en guías de onda mono- y multicapa de grafeno. Se establece una conexión entre este fenómeno y la capacidad cuántica intrínseca del material, y se estudia cómo afecta a las propiedades electromagneticas del grafeno en la banda de THz. Se han desarrollado circuitos equivalentes capaces de modelar la propagación de plasmones en estas estructuras, proporcionando una importante comprensión de los diferentes mecanismos de propagación una herramienta útil para el diseño de dispositivos. Por último, se analizan mediante ejemplos numéricos las implicaciones prácticas de la dispersión espacial en la respuesta de los filtros diseñados.

| Degree | Master in Telecommunication Engineering |
|---|---|
| Department | Information and Communication Technologies |
| Submission date | June 2015 |

# Contents

# Introduction

## 1.1 Terahertz Science and Technology

Terahertz radiation, loosely defined by the frequency range of 0.1 THz to 10 THz, has potential application in a plethora of fields, including material characterization, tomographic imaging, space science and communications, sensing, chemistry, biology, explosives inspection, integrated circuit testing, skin-cancer diagnosis, security, physics or broadband picocell communications [1].

However, THz waves are difficult to handle and cannot be treated with the well developed and mature techniques from the microwaves and optics. In this frequency range, electronic and optical phenomena combine, and a multi-perspective approach is required in order to develop effective devices. Unfortunately, current technology is unable to provide satisfactory results, and great efforts are being made towards filling the "THz Gap". Realizing efficient THz sources and detectors remains an unsolved problem that severely limits the viability of most applications, and the typical metallic and dielectric guiding structures from the neighbouring bands lead to prohibitively high losses and manufacture issues.

However, important advances have been made recently in THz sources and there is currently a variety of possibilities being intensively researched, each with its advantages and shortcomings. Sources can be broadly classified as either incoherent thermal sources, broadband pulse techniques, or narrowband methods [1, 2]. Broadband sources are based on the excitation of specific materials with ultrashort laser pulses (femtosecond pulses), enabling the generation of THz power through phenom-

ena such as non-linear effects in crystals or plasma oscillations [2]. Narrowband THz generation is done by frequency up-conversion from microwave oscillators through Schottky-diode multipliers, or directly from gas or semiconductor lasers, which tend to be very voluminous.

A large motivation for the development of THz technology is related to the potential to analyse materials through spectroscopy, to extract information that is unavailable when using other frequencies, especially from lightweight molecules and semiconductors [2]. Astronomy has traditionally been the main driving force behind the development of this field, because of the vast amount of information available through the study of molecules such as carbon monoxide, water, and oxygen in stellar bodies. This is crucial in space exploration and in the monitoring of atmospheric gases. In recent years, THz spectroscopy is also being applied in a much wider range of fields, from fundamental materials science to quality assurance of commercial products. Imaging with THz waves also has multiple pratical applications, since THz radiation penetrates materials that are opaque to light, and give a much higher resolution than microwaves. THz imaging has been succesfully used in cancer diagnosis due to unusual interactions with cancer cells (and other types of tissue), and nanoscale resolution is expected in recent years from near-field THz microscopy [1]. In the communication and information sector, there is an unexploited large potential market, since unpredecented wireless bandwidth may be achieved over short distances with THz technologies. These are merely a few critical applications of the THz spectrum, but it is clear that there is an urgent need of more efficient THz sources, more sensitive detectos, and better fundamental passive electrooptic components. This project aims to make a contribution to the latter field, through the utilization of graphene plasmonics.

## 1.2 Graphene plasmonics for THz applications

Surface plasmon polaritons (SPPs, or simply plasmons hereafter), the collective oscillations of surface charges, usually occur at the interface between materials with different-signed permittivity values and are commonly observed in optics at metal-dielectric interfaces. Over the past decades, metal plasmons have been an important subfield of photonics, and they current constitute the foundation for applications

such as integrated photonic systems, nanostructures, single photon transistors, or biosensing [3]. Metal plasmons do not exist as such at low THz frequencies, due to the non negative dielectric function of noble metals in this band, but composite structures have been reported to support localized surface plasmons [4, 5]. More recently, graphene has emerged as a promising candidate to fill this gap. Extensive theoretical works have been published in the span of a few years, and graphene plasmons have been experimentally observed by several groups [6, 7, 8, 9, 10]. This technology holds great promise as a platform for the effective manipulation of THz radiation at the nanoscale, with immediate application in various scientific fields. The explosive growth of graphene plasmonics is motivated by its true 2D nature (graphene is 1 atom thick) and the extraordinary electrooptical properties of this carbon allotrope [11]. Graphene is a semi-metal, characterized by a linear, conical energy dispersion and high carrier mobility, with a Fermi velocity $v_F \approx 10^6$ light, and its conductivity can be controlled via electrostatic gating or chemical doping. Free electrons or holes can be induced through moderate bias voltages, resulting in a control over charge concentrations not possible with metals. Typical doping concentrations of up to $1 \times 10^{13}$ cm$^{-2}$ can be achieved with relative ease, which translates to a chemical potential $\mu_c \approx 1$ eV [12, 13]. This enables unprecedented control over the plasmon modes supported by graphene guiding structures and extreme confinement of waves.

In this context, this project proposes novel graphene lowpass filters with reconfiguration capabilities that are not found with the current state of the art in this frequency range (chapter 2), and studies non-local electromagnetic effects in graphene at THz frequencies (chapter 3). Simple yet rigourous studies shed light into the fundamental physics of this complex phenomenon, and simple equivalent transmission line models are developed to accurately predict the behaviour of graphene SPPs when local models fail. In electromagnetics, graphene is typically studied through its surface conductivity $\sigma$, which is dependent on temperature, chemical potential, frequency, and a phenomenological carrier relaxation time that accounts for plasmon loss, mainly caused by charged impurities, lattice defects, and electron-phonon scattering [14]. In the semiclassical (local) model and in the absence of magnetic bias [15] $\sigma$ is independent of the wavevector $k_\rho$, and it can be modeled using the

Kubo formalism [16, 17] as

$$
\begin{aligned}
\sigma_{local} = \sigma_r - j\sigma_i = \\
-j\frac{e^2 k_B T}{\pi\hbar^2(\omega - j\tau^{-1})}\ln\left\{2\left[1 + \cosh\left(\frac{\mu_c}{k_B T}\right)\right]\right\},
\end{aligned}
\tag{1.1}
$$

where $\tau$ is the electron relaxation time, $\omega$ is the angular frequency, $e$ is the charge of an electron, $\hbar$ is the reduced Planck's constant, $T$ is temperature, $k_B$ is Boltzmann's constant, and $\mu_c$ is the chemical potential. Note that Eq. (1.1) only takes into account intraband contributions of graphene conductivity and thus is accurate up to tens of THz [18], as interband contributions are only significant when photon energy is near and above $2|\mu_c|$. For energies higher than this value, i.e. $\hbar\omega > 2|\mu_c|$, interband transitions from valence electrons dominate [19, 20].

# Chapter 2

# Graphene-based reconfigurable THz filters

In this chapter we propose the concept, synthesis, analysis, and design of graphene-based planar, plasmonic low-pass filters operating in the THz band. The proposed filters will be hosted in simple graphene waveguide configurations that allow straightforward biasing schemes, but the proposed design technique can be adapted in a straightforward manner to other graphene plasmonic waveguides, potentially combining graphene plasmonics with other technologies such as metamaterials or bidimensional metasurfaces to optimize performance. Such challenges lie outside the scope of this document, but would indubitably make for valuable and interesting research.

Currently, graphene-based plasmonic components ranging from waveguides [9, 21, 22, 15], antennas [23, 24, 25, 26, 27], reflectarrays [28], amplifiers [29], switches [30], modulators [31], or phase-shifters [32] to sensors [33, 34] have already been proposed and investigated. These devices may find application in different areas such as chemical and biological remote sensing, high resolution imaging and tomography, time-domain spectroscopy, atmospheric monitoring, and broadband picocellular or intrasatellite communication networks [35, 36, 37, 38].

Terahertz systems also require filtering elements to select target frequency bands and reject thermal radiation that may otherwise saturate sensitive detectors [39, 40]. Several types of THz filters can be found in the literature, such as low pass [41], high-pass [42], band-pass [43], and band-stop filters [44]. However, these implementations are based on bulky and heavy quasi-optical components that cannot be tuned electrically. In addition, planar plasmonic guided filter have been developed using noble metals [45, 46, 47], but they can operate only at optics and infrared frequencies.
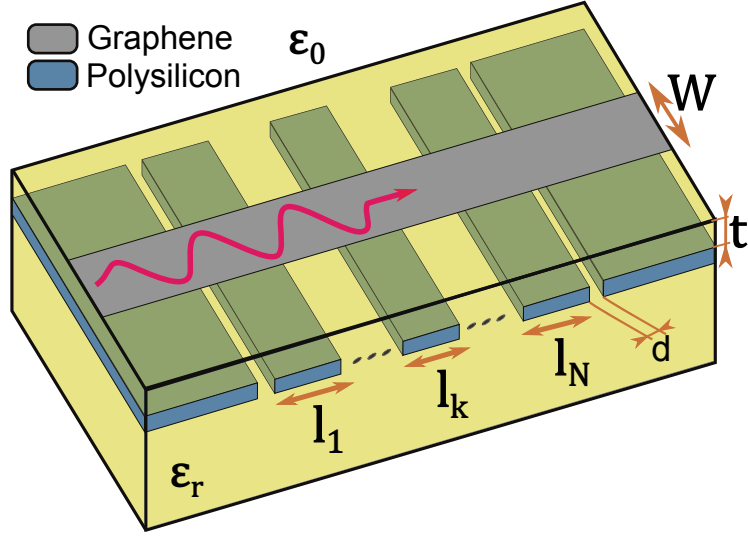
**Figure 2.1:** Proposed graphene-based THz low pass filter of $N^{th}$ degree. The structure consists of a monolayer graphene strip, with width $W$, and $N$ gating pads located beneath it.

Consequently, there is a clear need to develop planar and miniaturized THz filters able to be integrated in future reconfigurable communications and sensing systems.

In this context, we propose the concept, analysis, and design of graphene-based THz plasmonic reconfigurable low-pass filters. The structure is composed of a graphene strip and several independent polysilicon DC gating pads located beneath it, as depicted in Fig. 2.1. The strip supports the propagation of extremely-confined transverse-magnetic (TM) plasmons [21, 22] whose guiding characteristics can be dynamically modified along the structure by applying different DC bias voltages to the gating pads. If all pads are equally biased, the structure behaves as a simple plasmonic transmission line (TL) propagating the input waves towards the output port. When a different DC bias is applied to a gating pad, the guiding properties of the strip area located above are modified thanks to graphene's field effect. We apply this concept to implement stepped impedance low pass filters, which are composed of a cascade of transmission lines alternating sections of high and low characteristic impedance. Importantly, the cutoff frequency of the filters can be dynamically tuned by simultaneously modifying the DC bias applied to the gates. A synthesis procedure is then presented to design filters with the desired cutoff frequency, in-band return loss, and rejection characteristics, directly providing the physical length of the gating pads and the required biasing voltages. The electromagnetic modeling of the structure is performed combining a transmission line model with

a transfer-matrix approach. To this purpose, a recently introduced graphene electrostatic scaling law [22] is applied to efficiently compute the propagation constant of the modes supported by the strip as a function of its width, surrounding media, and applied electrostatic DC bias. The proposed approach allows the accurate analysis of the desired filters in just seconds, avoiding large simulation times of general purpose full-wave software.

The fabrication of the proposed filters could be carried out through standard e-beam lithography techniques, and the coupling of power to the structure may be accomplished through several recently developed techniques for the excitation of SPPs in graphene [26, 27, 48, 49, 50, 51, 52, 53, 54]. Rapid advancements are occurring in these areas, and the proposed filters may represent an important step towards innovative THz communication solutions as a key constituting element of future THz plasmonic systems.

In order to illustrate these concepts, several low-pass filters are designed and analyzed, evaluating their performance and reconfiguration capabilities in the THz band. In addition, some practical considerations concerning the implementation of the proposed filters are addressed, discussing in detail the real gating structure and the influence of graphene's losses in the filters performance.

## 2.1   Proposed Structure

The proposed structure, depicted in Fig. 2.1, comprises a graphene ribbon transferred onto a dielectric substrate and a number of polysilicon gating pads beneath the strip.

Graphene's surface conductivity is modeled through Kubo's formalism, as introduced in Chapter 1. One of the most interesting features of graphene is that its chemical potential can be tuned over a wide range (typically from -1 eV to 1 eV) by applying a transverse electric field via a DC biased structure, such as the one proposed here. An approximate closed-form expression to relate $\mu_c$ and the applied DC voltage ($V_{DC}$), is given by

$$\mu_c \approx \hbar v_F \sqrt{\frac{\pi C_{ox}(V_{DC} - V_{Dirac})}{e}}, \tag{2.1}$$

where $V_{Dirac}$ is the voltage at the Dirac point, $C_{ox} \approx \varepsilon_r \varepsilon_0 / t$ is the gate capacitance
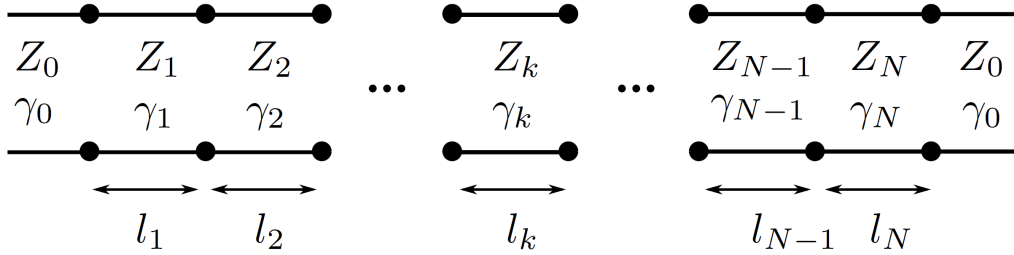
**Figure 2.2:** Equivalent TL model of the graphene-based filter shown in Fig 2.1.

using the standard parallel-plate approximation, $\varepsilon_r$ and $t$ are the permittivity and thickness of the gate dielectric, and $v_F$ is the Fermi velocity in graphene ($v_F \approx 10^6$). In addition, graphene monolayers support the propagation of surface plasmons polaritons at THz frequencies with moderate losses and extreme confinement. Several authors have studied the characteristics of the SPPs propagating along graphene ribbons [21, 22],

and transmission line models have been successfully utilized to describe this type of structure [29, 55, 56]. Using this approach, the structure of Fig. 2.1 can be modeled as a cascade of transmission lines, as shown in Fig. 2.2. The complex-valued characteristic impedance and propagation constant of the transmission lines depend on graphene's chemical potential, and can be largely modified by the DC voltage applied to the gating pads, allowing the synthesis of the proposed filters.

## 2.2 Synthesis and Modeling of Graphene-based Lowpass Filters

### 2.2.1 Synthesis Procedure

The goal of this section is to design a lowpass filter using the structure of Fig. 2.1, with the desired cutoff frequency, rejection characteristics, and inband performance. This structure implements a so-called stepped impedance lowpass filter [57], whose equivalent network is presented in Fig. 2.2. As seen, it is composed of the connection of $N$ transmission line sections with lengths $l_k$, propagation constants $\gamma_k$, and characteristic impedances $Z_k$. The design procedure starts with the calculation of a set of characteristic polynomials able to satisfy the desired specifications in terms of in-band and out-of-band characteristics. Scattering parameters are expressed in

terms of these polynomials as follows

$$S_{21}(\omega) = \frac{1}{\varepsilon E(\omega)} \quad \text{and} \quad S_{11} = \frac{F(\omega)}{E(\omega)}. \tag{2.2}$$

The calculation of the $F(\omega)$ and $E(\omega)$ polynomials is done analytically for most useful transfer functions, including Butterworth and generalized Chebyshev responses. Some useful techniques are reported in [57]. The next step in the design procedure is the election of the electrical length $\theta_c$ of the individual line sections. This parameter directly determines the periodicity of the frequency response when the ideal polynomials are implemented with transmission lines. Smaller values of $\theta_c$ result in a wider spurious-free range, while requiring more abrupt changes in the line impedances. Having decided the value of $\theta_c$, a recursive technique [57] is applied to extract the normalized values of characteristic impedances $(\bar{Z}_k)$. Then, the de-normalization of the calculated characteristic impedances to the real port impedances $(Z_0)$ used in the filter implementation is done as $Z_k = \bar{Z}_k Z_0$.

The final and crucial design step consists in finding the design parameters of the physical structure in Fig. 2.1, to implement the prototype circuit at the desired cut-off frequency. To this purpose, the required de-normalized impedance values $(Z_k)$ obtained during the above procedure are synthesized using the SPP properties of graphene strips. This can be most efficiently accomplished by appropriately adjusting the chemical potential $(\mu_c)$ along the strip through electrostatic gating. As an illustrative example of this electrical control, we show in Fig. 2.3 the real part of the characteristic impedance and normalized phase constant of the first waveguide-like mode propagating along a graphene strip, computed versus the chemical potential for graphene strips of different characteristics. It can be observed in the figure that, for several strip widths and frequencies, the impedances achievable vary from around 20 k$\Omega$ to several hundreds of ohms for practical chemical potentials in the range $0-1$ eV. Importantly, the calculation of the chemical potentials for all sections also fixes the values of their propagation constants $(\beta_k)$. This information, combined with the election of $\theta_c$ done during the synthesis phase, allows the calculation of the physical lengths of all graphene strip sections in Fig. 2.1 using the straightforward relation

$$l_k = \frac{\theta_c}{\beta_k(\mu_c)}. \tag{2.3}$$

Note that this synthesis procedure is only strictly valid when lossless transmission
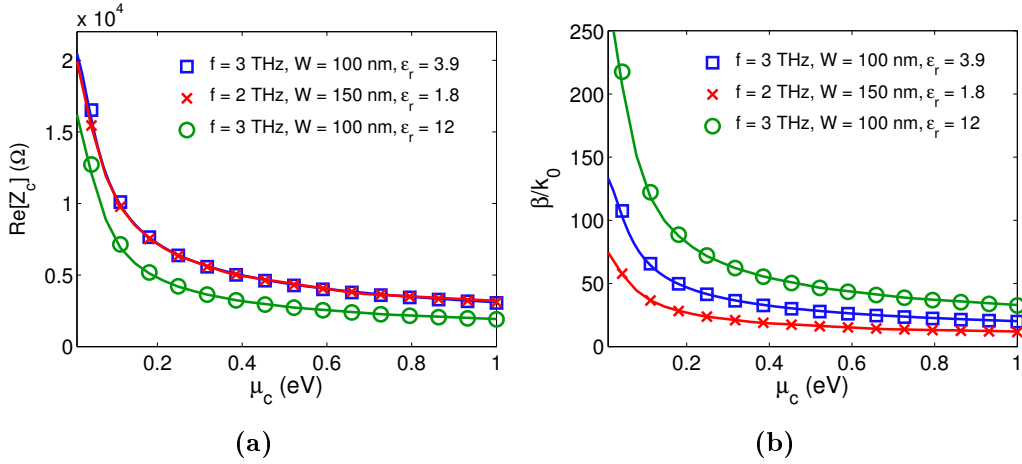
**Figure 2.3:** Characteristic impedance (a) and normalized phase constant (b) of the first waveguide-like surface plasmon propagating along different graphene strip configurations versus the chemical potential $\mu_c$. Solid lines have been obtained using the electrostatic approach described in Section 2.2.2, and markers indicate values computed with HFSS. Graphene parameters are $\tau = 1$ ps and $T = 300$ K.

lines are considered. The presence of losses in the real structure leads to small deviations between the actual filter response and the expected synthesized function [57], adding some extra round-off inside the filter passband. Also, the connection of transmission lines of different characteristic impedances is considered to be ideal. In practice, the presence of real gating pads has some influence on the propagation characteristics of the SPP modes propagating along the different graphene strip sections. All these non-ideal effects will be discussed in the last section of the chapter.

## 2.2.2   Electromagnetic Modeling

The electromagnetic modeling of the structure shown in Fig. 2.1 is based on the analysis of its equivalent network (see Fig. 2.2) using a transmission line formalism combined with an ABCD transfer-matrix approach [58].

For the sake of brevity, the details of the synthesis procedure and the numerical examples shown throughout this chapter will focus solely on a graphene strip of arbitrary width. By the end of this chapter, the potential design of filters in other host graphene waveguides will become apparent to the reader. For sufficiently wide strips, i.e. $W \gg \lambda_{spp}$, all features of the fundamental SPP mode can be analytically

calculated assuming a laterally infinite waveguide [59], greatly simplifying the design and study of these filters. Unfortunately, narrow strips of a few dozens or hundreds of nanometers, which may be more useful for highly miniaturized integrated THz transceivers, do not allow this luxury [21, 22], and one has to resort to full-wave numerical techniques. Consequently, the use of a transmission line model in this case would generally require the numerical analysis of the propagating modes along multiple isolated graphene strips of varying characteristics, which remains a computationally costly task. This shortcoming, however, can be elegantly overcome by making use of the quasi-electrostatic nature of surface plasmons in narrow graphene strips, enabling an extremely efficient design and analysis tool. To this end, the scaling law proposed in [22], based in the quasi-electrostatic nature of surface plasmons in graphene strips, will be used. This approach, which assumes that the strip width is much smaller than the wavelength, establishes that plasmon properties are solely determined by the strip width ($W$), surrounding media ($\varepsilon_r$), and graphene conductivity ($\sigma$). Then, once the propagating features of a given plasmonic mode have been obtained, they can be scaled to any arbitrary strip by using the scaling parameter

$$\eta(\beta, W) = \frac{\text{Im}[\sigma(f_\beta)]}{f_\beta W \varepsilon_{eff}}, \tag{2.4}$$

where $f_\beta$ is the frequency where the surface plasmon propagates with a phase constant $\beta$, and $\varepsilon_{eff} = (1 + \varepsilon_r)/2$ models the dielectric media. Note that, due to the electrostatic approach employed to derive Eq. 2.4 (see [22]), the scaling parameter $\eta$ is independent of the operation frequency.

This scaling law is applied to efficiently compute the SPP propagating features along any graphene strip. The process is as follows. First, the scaling parameter $\eta$ related to the desired surface mode is obtained using a *single* full-wave simulation. Note that this simulation is performed only once, and the $\eta - \beta W$ curve computed will be employed for the design of any filter, regardless of the strip width, graphene conductivity, or supporting substrate. Fig. 2.4 confirms that $\eta$ only depends on the product $\beta W$ [22] and that surface plasmons propagating on different strips lead to the same scaling parameter. Second, the phase constants of surface plasmons propagating along strips of arbitrary characteristics are computed using $\eta$. To this purpose, the scaling parameter is computed at the desired operation frequency $f_\beta$
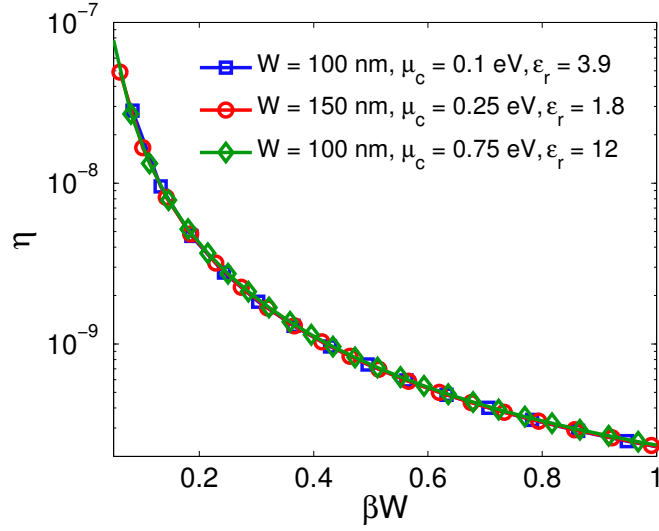
**Figure 2.4:** Scaling parameter $\eta$ versus the product of the phase constant and the strip width ($\beta W$) for different graphene strip configurations. Graphene parameters are $\tau = 1$ ps and $T = 300$ K.

and strip width $W$ using Eq. 2.4, and the corresponding value of $\beta$ is then retrieved using the information of Fig. 2.4. Finally, the attenuation constant is found as $\alpha = 1/(2L_p)$, where $L_p$ is the $1/e$ decay distance of the power. The propagation distance of plasmons ($L_p$) is mainly controlled by the electron relaxation time of graphene $\tau$, and it can be approximately obtained by $v_g \tau$, where $v_g$ is the plasmon's group velocity ($v_g = \mathrm{d}\omega_p/\mathrm{d}\beta$) [22]. Therefore, the attenuation constant may be expressed as

$$\alpha = \frac{1}{2v_g \tau}. \tag{2.5}$$

Once the complex propagation constant $\gamma = \alpha + j\beta$ of the propagating TM plasmon is known, its characteristic impedance is obtained as [58]

$$Z_C = \frac{\gamma}{j\omega\varepsilon_0\varepsilon_{eff}}. \tag{2.6}$$

The accuracy of this approach is validated in Fig. 2.3, where the characteristic impedance and phase constant of plasmons propagating along different strip configurations are computed using both the proposed technique and the finite element method (FEM) software Ansoft HFSS. There, the graphene strip is modeled as an infinitesimally thin layer where surface impedance boundary conditions are imposed ($Z_{surf} = 1/\sigma$).

The combination of the graphene strip scaling law with a transmission line and transfer-matrix approach permits an extremely fast electromagnetic analysis of the proposed filtering structure (see Fig. 2.1), allowing an efficient implementation of the synthesis technique described in the previous section.

## 2.3    Design Examples

In this section we design and analyze two low-pass filters implemented using the structure shown Fig. 2.1. For the sake of generality, the filters have been designed to have different order and cutoff frequencies, considering various strip widths and dielectrics. The performance of the filters is presented in terms of their scattering parameters, referred to the characteristic impedance of the graphene sections at the input and output ports. A comparison between the transmission line model combined with the scaling law and full-wave results using HFSS is shown for both cases, validating the accuracy of the proposed electromagnetic modeling. In addition, the reconfiguration capabilities of the filters are investigated in detail. In this study, we consider a temperature of $T = 300$ K and graphene with a relaxation time $\tau$ of 1 ps, which corresponds approximately to a carrier mobility of 50000 $cm^2/(Vs)$ for a chemical potential of $\mu_c = 0.2$ eV [60]. Here we focus on the filtering performance of the proposed structures, whereas other practical considerations, such as the presence of the gating pads and their effect on the filter performance, or the influence of losses, will be discussed in the next section.

In the first example, we consider a graphene strip of 150 nm transferred onto a dielectric of relative permittivity 1.8, e.g. ion gel [60]. Using this host waveguide, we have designed a $7^{th}$ degree filter with a cutoff frequency of 2.3 THz. The Chebyshev polynomials were computed using standard techniques [57] for a maximum theoretical return loss of 30 dB, and the electrical length $\theta_c$ at the cutoff frequency was set to 37°. These values were chosen to yield practical values of chemical potential through the synthesis procedure explained in the previous section. The final design parameters of the filter are shown in Table 2.1. Note that filters of this degree with better roll-off characteristics could be synthesized, but this would further increase the required range of chemical potential values achievable in the structure.

Fig. 2.5a shows the frequency response of the filter, computed using the proposed

**Table 2.1:** Design parameters of the first example: a 7th degree filter.

| Section | $\bar{Z}$ | $l$ (nm) | $\mu_{c,nominal}$ (eV) | $\mu_{c,tuned1}$ (eV) | $\mu_{c,tuned2}$ (eV) |
|---------|-----------|----------|------------------------|------------------------|------------------------|
| Ports | 1 | 500 | 0.17 | 0.27 | 0.41 |
| 1,7 | 1.37 | 382 | 0.1 | 0.15 | 0.23 |
| 2,6 | 0.57 | 929 | 0.51 | 0.74 | 1 |
| 3,5 | 2.26 | 232 | 0.026 | 0.06 | 0.1 |
| 4 | 0.45 | 1172 | 0.79 | 1 | 1 |



(a)          (b)
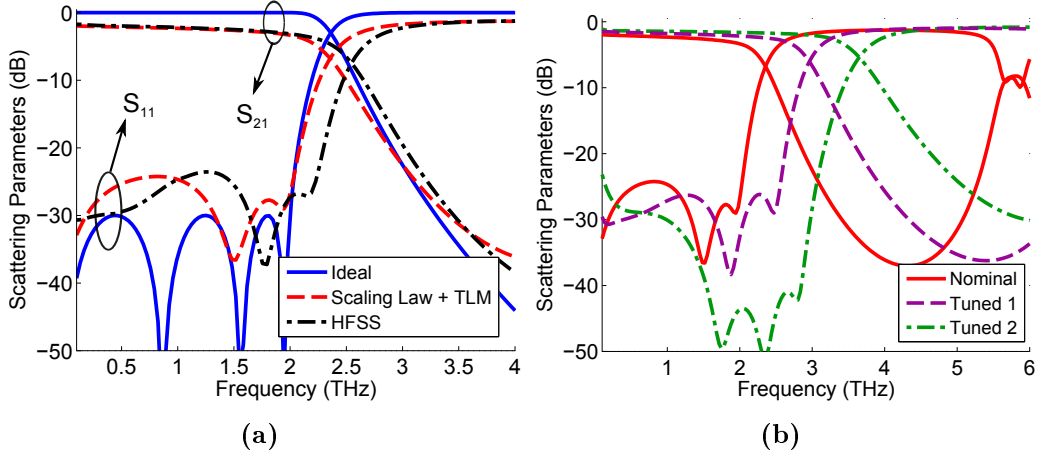
**Figure 2.5:** Scattering parameters of a $7^{th}$ degree filter implemented using the structure depicted in Fig. 2.1. The design parameters are shown in Table 2.1, the strip width is 150 nm, and a dielectric of $\varepsilon_r = 1.8$ is employed as a substrate. (a) Nominal filter designed to have a cutoff frequency of 2.3 THz. Results are obtained using the ideal synthesis procedure, the transmission line approach combined with the scaling law, and the commercial software HFSS. (b) Reconfiguration possibilities of the filter obtained by adequately controlling the DC bias of the different gating pads.

transmission line approach and the full-wave commercial software HFSS. A good degree of agreement is observed, with very similar attenuation profile and average level of return loss in the passband. Moreover, the structure presents a low insertion loss level, around 3 dB, which is a remarkable value at this frequency range. The slight difference in the cutoff frequency between both approaches is due to the mono-modal nature of the transmission line approach, which neglects higher order effects at the connection between two adjacent graphene strip sections. This results in small modifications in the phase condition of the circuit, which is now fulfilled at a slightly different cutoff frequency. Interestingly, this effect appears to be uniform along the structure, allowing to adjust the filter's cutoff frequency by a small overall

**Table 2.2:** Design parameters of the second example: a 9th degree filter.

| Section | $\bar{Z}$ | $l$ (nm) | $\mu_{c,nominal}$ (eV) | $\mu_{c,tuned1}$ (eV) | $\mu_{c,tuned2}$ (eV) |
|---|---|---|---|---|---|
| Ports | 1 | 200 | 0.17 | 0.35 | 0.46 |
| 1,9 | 1.36 | 156 | 0.1 | 0.21 | 0.274 |
| 2,8 | 0.58 | 367 | 0.43 | 0.93 | 1 |
| 3,7 | 2.24 | 94 | 0.035 | 0.01 | 0.12 |
| 4,6 | 0.44 | 483 | 0.69 | 1 | 1 |
| 5 | 2.48 | 85 | 0.023 | 0.078 | 0.1 |

scaling of the section lengths. Fig. 2.5b illustrates the reconfiguration possibilities of the designed filter. By adequately controlling the DC voltage applied to the gating pads, following the synthesis procedure described in Section 2.2.1, the overall electrical length of the device can be modified thus leading to an electric control of the filter's cutoff frequency. For the sake of clarity, only two additional possible reconfiguration states are shown in the figure (their corresponding design parameters are shown in Table 2.1). However, a continuous range of cutoff frequencies can be easily synthesized. Importantly, the proposed filter allows a dynamic control of the cutoff frequency over 50%. This value is mainly limited by two factors. First, the fixed physical length of the gating pads imposes a limit to the maximum frequency shift attainable while maintaining an acceptable variation of the attenuation profile and return loss. Second, the values of the chemical potential employed are limited, by technological reasons [61], to the range of $0 - 1$ eV.

The second example is composed of a strip of width $W = 100$ nm transferred onto a quartz substrate of $\varepsilon_r = 3.9$. The filter's degree has been increased to $N = 9$ and the cutoff frequency is set to 3.3 THz, with $\theta_c = 39°$. The complete design parameters of the filter are shown in Table 2.2 and the frequency response is plotted in Fig. 2.6a. Very similar conclusions compared to the previous design can be drawn from the filter response. Importantly, the small difference in the cutoff frequency between the two electromagnetic analysis is also of similar relative magnitude to that of the previous example. Finally, the tunable features of this filter are shown in Fig. 2.6b, where around 50% of cutoff frequency dynamic control is again obtained.
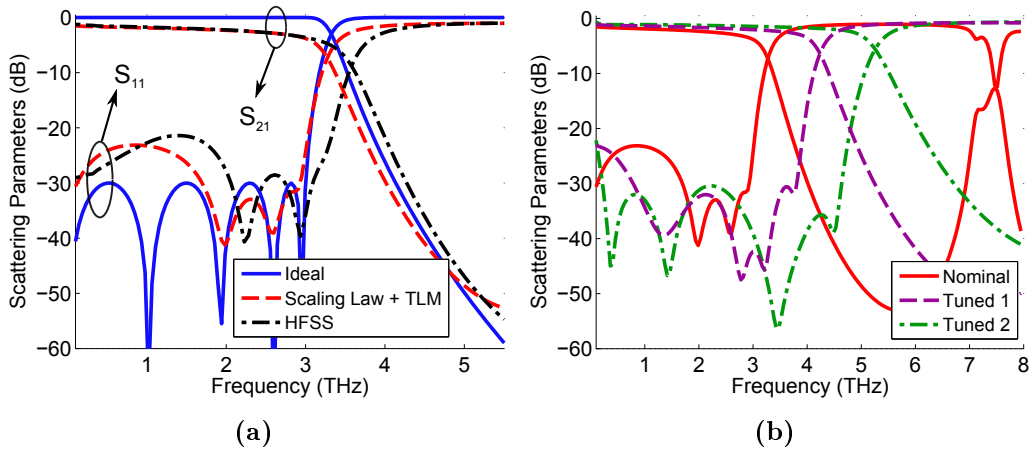
**Figure 2.6:** Scattering parameters of a $9^{th}$ degree filter implemented using the structure depicted in Fig. 2.1. The design parameters are shown in Table 2.2, the strip width is 100 nm, and a dielectric of $\varepsilon_r = 3.9$ is used as substrate. (a) Nominal filter designed to have a cutoff frequency of 3.3 THz. Results are obtained using the ideal synthesis procedure, the transmission line approach combined with the scaling law, and the commercial software HFSS. (b) Reconfiguration possibilities of the filter obtained by adequately controlling the DC bias of the different gating pads.

## 2.4 Practical Considerations

This section briefly discusses several technological aspects related to the possible practical implementation of the proposed filters, such as the strip biasing and the influence of graphene losses.

### 2.4.1 Rigourous electrostatic biasing of graphene strips

The results presented in previous section assumed, as a first approximation, an ideal carrier distribution along the graphene strip. However, this distribution requires strong discontinuities between adjacent sections. In practice, this carrier density profile cannot be achieved because i) there is a physical space between two adjacent gating pads (see Fig. 2.1), and ii) there are fringing effects at the edges of the gating pads, which may modify the carrier density profile. Here, we show that good performance is maintained after rigourously considering these effects.

The analysis of the filter is performed in two different steps. First, a electrostatic study is performed in order to determine the real carrier density profile induced on the graphene strip by the different gating pads. Then, this carrier density is employed to compute the electromagnetic behavior of the filter, as detailed in Section

**Table 2.3:** Gate Voltages for the $7^{th}$ degree filter

| Section | ports | 1,7 | 2,6 | 3,5 | 4 |
|---|---|---|---|---|---|
| Initial Voltage (V) | 5.4 | 1.9 | 48.4 | 0.13 | 116 |
| Optimized Voltage (V) | 5.4 | 1.8 | 40 | 0.1 | 90 |

**Table 2.4:** Gate Voltages for the $9^{th}$ degree filter

| Section | ports | 1,9 | 2,8 | 3,7 | 4,6 | 5 |
|---|---|---|---|---|---|---|
| Initial Voltage (V) | 2.5 | 0.86 | 15.9 | 0.11 | 41 | 0.05 |
| Optimized Voltage (V) | 2.5 | 0.68 | 12 | 0.06 | 31 | 0.05 |

III. The electrostatic problem has been solved using the commercial software AN-SYS Maxwell, considering that the graphene strip is connected to the ground, and assigning adequate biasing voltages to the different gating pads. These voltages are initially computed with Eq. 2.1 to provide the ideal values of chemical potential. The gating pads are placed 25 nm below the graphene strip and 35 nm apart from adjacent pads ($t = 25$ nm and $d = 35$ nm in Fig. 2.1), with a pad thickness of 50 nm. This approach allows to obtain the charge distribution at the graphene-substrate interface, $\rho(z)$, which in turn permits computing the real distribution of chemical potential along the strip as [62]

$$\mu_c(z) = \frac{\hbar v_F}{e} \sqrt{\frac{\pi \rho(z)}{e}}. \tag{2.7}$$

Once the chemical potential is known, the complex-valued conductivity at each point of the strip is computed with (1.1). Due to the finite distance between pads and the effect of fringing DC fields, using the initial voltages computed with Eq. 2.1 may result in a filter with a shifted frequency response, requiring an additional optimization step. Tables 2.3-2.4 show the initial and optimized values of voltage assuming no previous chemical doping. Figs. 2.7a-2.7b depict the chemical potential profile along the strip computed with this approach for the filters proposed in the previous section.

Note that filters with lower gate voltages can be easily designed by setting a more relaxed initial specification, specifically by increasing the electrical length of the transmission line sections ($\theta_c$) in the synthesis of the polynomials. However, this comes at the expense of a worse spurious free range in the final filter.

Once the electrostatic problem has been solved, we analyze the EM response

22
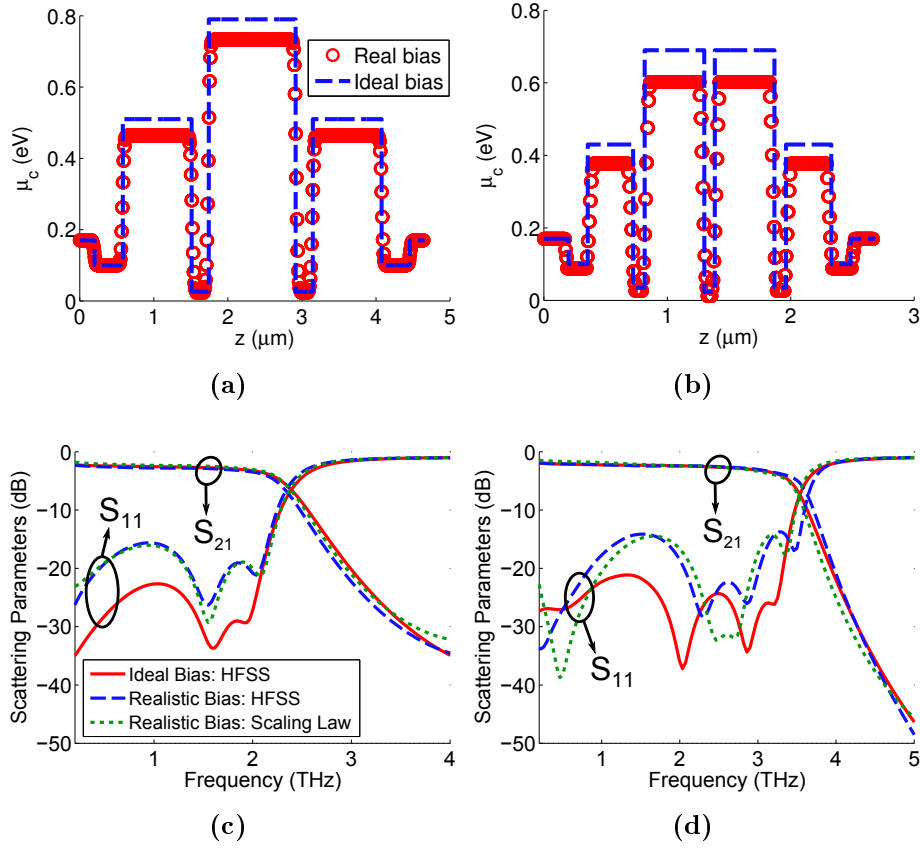
**Figure 2.7:** Comparison between ideal and realistic longitudinal chemical potential distributions of the (a) $7^{th}$ and (b) $9^{th}$ degree filters. (c) and (d) show the frequency response of the resulting filters computed using the transmission line approach combined with the scaling law, and the commercial software HFSS.

of the proposed structures taking into account the presence of the gating pads, which can be modelled at THz frequencies as a dielectric with permittivity $\varepsilon_r \approx 3$ [26, 27, 63]. The inclusion of the gating pads in the dynamic analysis barely affects the EM response of the filters, because they are electrically very thin and with relative permittivity very similar to the background substrate. Figs. 2.7c-2.7d show the frequency response of these filters, computed via full-wave simulations and with the the scaling law, obtaining again good accuracy while requiring negligible computational resources. This study further confirms the robustness and usefulness of the proposed analysis technique, since performing full-wave analysis of continuously varying conductivity profiles is a tedious and time-consuming process. The overall performance of both filters remains satisfactory, despite the slight deterioration of the in-band reflection profile. This effect is caused by the smooth transitions in the
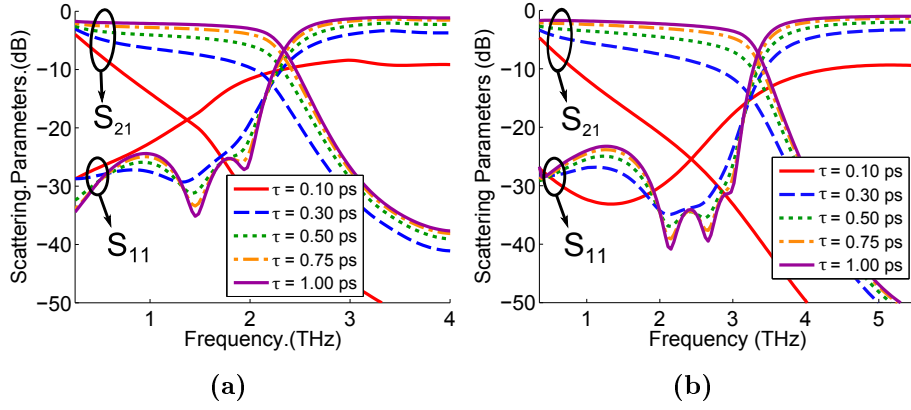
**Figure 2.8:** Influence of graphene's relaxation time in the frequency response of the (a) $7^{th}$ and (b) $9^{th}$ degree filters.

spatial distribution of chemical potential, not accounted for in prototype network, and is more severe in the $9^{th}$ degree filter due to very strong and narrow variation of conductivity in the central sections of the filter. This known limitation of stepped impedance low-pass filters [57] could be overcome by implementing more complex circuits that use impedance inverters or lumped elements to account for higher order effects at the junctions.

## 2.4.2   Influence of Graphene losses

The presence of potentially high losses is an important factor to take into account while evaluating the performance of the proposed filters. To assess this point, the $7^{th}$ and $9^{th}$ degree filters have been analysed assuming different values of graphene relaxation time ($\tau$). Figs. 2.8a-2.8a show the frequency response of both filters for values of $\tau$ ranging from 0.1 ps to 1 ps. It is observed that graphene's relaxation time strongly affects the insertion loss of the filter and the sharpness of the transition between the pass-band and the rejected band. For relaxation times as low as $\tau = 0.1$ ps, losses are too high for the filter to present practical utility, whereas values nearing 0.5 ps and above show very good performance. Importantly, values of electron mobility in graphene on a boron nitride substrate of up to 40000 $cm^2/Vs$, which corresponds to $\tau \approx 0.8$ ps, have been experimentally observed at room temperature [64]. This measured value confirms that the proposed filters are of practical value using state of the art graphene technology.

# Chapter 3

# Spatial Dispersion in Graphene: Equivalent Circuits and Effect on Device Performance

As discussed in previous chapters, the propagation of surface waves along graphene-based structures has attracted significant attention at microwaves, millimeter-waves, and low THz frequencies [9, 15, 65, 66]. This has led to a plethora of exciting theoretical research on graphene-based devices, like the THz-infrared lowpass filters proposed in the previous chapter. However, the possible influence of spatial dispersion in the propagation characteristics of surface plasmons in graphene has usually been neglected, and a clear interpretation of this phenomenon, for instance in terms of equivalent simple circuit models, is still missing.

Recent studies have demonstrated that spatial-dispersion may significantly affect the propagation of surface plasmons in graphene-based strips and 2D waveguides even at the very low THz regime [67, 68, 18]. Initial works [67, 68] were based on a *low-$k_\rho$* conductivity model based on the relaxation-time approximation (RTA) [69], which is accurate up to the THz band (it only considers intraband contributions) for sufficiently fast surface waves. However, spatial dispersion becomes especially important for extremely slow-waves [67], a scenario in which this approximate model is not strictly valid [69]. Note that although the excitation of surface plasmons in graphene is difficult due to the large momentum mismatch between plasmons and incoming electromagnetic waves, different techniques have already been successfully
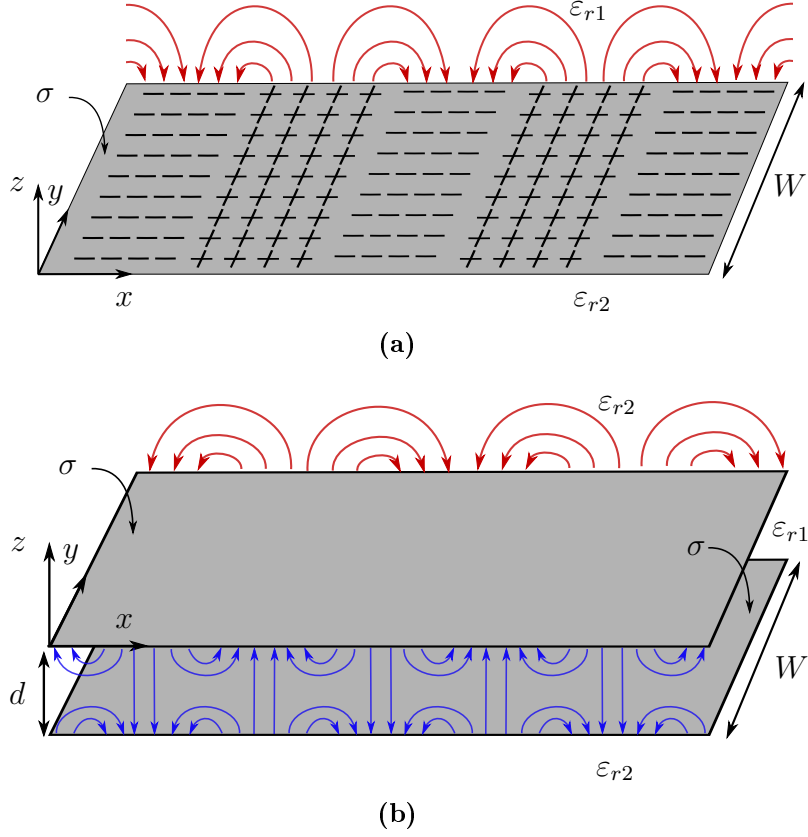
**Figure 3.1:** Graphene-based waveguides. (a) Single graphene sheet. The figure shows the charge distribution and electric field of a surface plasmon propagating on the sheet. (b) Graphene-based parallel-plate waveguide. The figure shows the field distributions of the dominant modes: odd quasi-TEM mode (blue) and even TM mode (red). The width of both waveguides is much larger than the guided wavelength, i.e. $W \gg 1/k_\rho$.

developed for this purpose [70, 71, 72, 26]. On the other hand, the use of equivalent circuits has recently been proposed to model wave propagation along graphene sheets [29, 55], similar to the case of plasmons along noble metals in optics [73]. The analytical relation between the circuit elements and graphene's conductivity [55] allows to clearly identify the different mechanisms involved in plasmon propagation, explaining their connection with the intrinsic properties of graphene. However, in contrast to carbon nanotubes [74], current equivalent circuit models cannot handle the propagation of surface plasmons along spatially dispersive graphene.

In this context, this chapter is dedicated to the study of graphene SPPs in spatially dispersive graphene-based 2D waveguides via analytical methods. First, a *full-$k_\rho$* RTA tensorial conductivity model [18] is used to derive the exact dispersion relation of the waveguides under study. These consist of a single graphene sheet and

a parallel-plate waveguide (PPW) (see Fig. 3.1). The *full-$k_\rho$* conductivity model provides accurate results for any plasmon wavenumber, and, since it considers intra-band contributions of graphene, it is valid up to infrared frequencies. Importantly, rigorous analytical expressions are provided for the first time to characterize surface plasmons propagation along a spatially dispersive graphene sheet. We demonstrate both analytically and numerically that spatial dispersion significantly decreases the mode confinement and the losses of extremely slow waves, which usually appear in practical waveguide structures composed of dielectrics with high permittivity values. Furthermore, we compare our results with previously reported studies [67, 68], confirming that in these scenarios, the use of a conductivity model able to handle large values of the wavenumber is required to accurately take the spatial dispersion phenomenon into account. The analytical results obtained using the RTA model are further validated numerically using the *full-$k_\rho$* Bhatnagar-Gross-Krook (BGK) conductivity model [18], which enforces charge conservation and is expected to be more accurate than the RTA model. Both approaches leads to extremely similar results, thus demonstrating the usefulness of the RTA-based analytical developments. However, note that due to the mathematical complexity of the BGK model, it cannot be applied to derive analytical expressions for the characteristics of graphene-based surface plasmons.

Second, we derive simple equivalent transmission line models able to model TM surface wave propagation along these waveguides, encapsulating all non-local effects into a shunt quantum capacitance exclusively dependent on the characteristics of graphene. Third, we discuss the implications of these findings in realistic devices, such as the filters studied in chapter 2.

## 3.1 RTA Non-Local Model for the Intraband Conductivity of Graphene

An analytical spatially dispersive model for the intraband conductivity tensor of graphene valid for arbitrarily wavevector values was derived [18] from the semiclassical Boltzmann transport equation under the relaxation-time approximation (RTA) and using a linear electron dispersion near the Dirac points. Using a cartesian co-

ordinate system $(x - y)$, this conductivity tensor can be expressed as

$$\overline{\overline{\sigma}}^{\text{RTA}} = \gamma \overline{\overline{I}}_\phi, \tag{3.1}$$

where

$$\gamma = -j \frac{e^2 k_B T}{\pi^2 \hbar^2} \log \left\{ 2 \left[ 1 + \cosh(\frac{\mu_c}{k_B T}) \right] \right\}, \tag{3.2}$$

and

$$I_{\phi xx}(k_x, k_y) = 2\pi \frac{v_F^2 k_y^2 k_\rho^2 R - \xi v_F k_x p^2 - \xi^2 p^2 (1 - R)}{v_F^2 (\xi + v_F k_x) k_\rho^4}, \tag{3.3}$$

$$I_{\phi yy}(k_x, k_y) = 2\pi \frac{v_F^2 k_x^2 k_\rho^2 R + \xi v_F k_x p^2 + \xi^2 p^2 (1 - R)}{v_F^2 (\xi + v_F k_x) k_\rho^4}, \tag{3.4}$$

$$\begin{aligned} I_{\phi xy}(k_x, k_y) = & I_{\phi yx}(k_x, k_y) = -2\pi k_x k_y \\ & \cdot \frac{v_F^2 k_\rho^2 R + 2\xi v_F k_x + \xi^2 p^2 (1 - R)}{v_F^2 (\xi + v_F k_x) k_\rho^4}, \end{aligned} \tag{3.5}$$

with $k_\rho^2 = k_x^2 + k_y^2$, $\xi = \omega - j\tau^{-1}$, $R(k_x, k_y) = \frac{\xi + v_F k_x}{\sqrt{\xi^2 - v_F^2 k^2}}$, and $p^2 = k_x^2 - k_y^2$.

Let us consider the case of a laterally infinite graphene sheet, which supports a surface wave with wavenumber $k_\rho$ propagating along the $x$-axis (see Fig. 3.1a). This sheet is isotropic in the $xy$ plane, which means that the relation between the electric field and the surface current does not depend on the orientation of the sheet in the plane [18]. Using this coordinate system, Eq. (3.1) can be expressed as

$$\overline{\overline{\sigma}} = \begin{pmatrix} \sigma_{xx} & 0 \\ 0 & \sigma_{yy} \end{pmatrix}, \tag{3.6}$$

where $\sigma_{xx} \neq \sigma_{yy}$ [18]. This reference system leads to non-equal diagonal terms of the conductivity tensor, which hinder the application of the approaches developed in [67, 68] to study plasmon propagating along laterally infinite graphene sheets.

In order to simplify the expressions of the conductivity model, we take advantage of the isotropic property of graphene sheets [18] to chose an specific reference system $(x' - y')$, where the axis $x'$ and $y'$ are rotated 45° with respect to the $\rho$ direction of the propagating wave. In this reference system the relations $k_{x'}^2 = k_{y'}^2$ and $k_\rho^2 = 2k_{x'}^2$ hold, which allows to simplify the conductivity tensor to

$$\sigma_{x'x'} = \sigma_{y'y'} = \gamma \frac{\pi}{\sqrt{(\omega - j\tau^{-1})^2 - v_F^2 k_\rho^2}}, \tag{3.7}$$

$$\sigma_{x'y'} = \sigma_{y'x'} = -\gamma\pi \left[ \frac{1}{\sqrt{\xi^2 - v_F^2 k_\rho^2}} + \right.$$

$$\frac{2\xi k_\rho/\sqrt{2}}{v_F(\xi + v_F(k_\rho/\sqrt{2}))k_\rho^2} + \tag{3.8}$$

$$\left. 2\xi^2 \frac{\sqrt{\xi^2 - v_F^2 k_\rho^2} + (\xi + v_F(k_\rho/\sqrt{2}))}{k_\rho^2(\xi + v_F(k_\rho/\sqrt{2}))\sqrt{\xi^2 - v_F^2 k_\rho^2}} \right].$$

Importantly, Eqs. (3.7)-(3.8) are expressed only as a function of the wavenumber $k_\rho$ and satisfy the desired symmetries [18] $\sigma_{x'x'} = \sigma_{y'y'}$ and $\sigma_{x'y'} = \sigma_{y'x'}$. These equations allow an easy treatment of laterally infinite graphene sheets following previously introduced approaches [67], [68]. In addition, it should be noted that a graphene sheet is isotropic in nature [18], and therefore the cross conductivity terms $\sigma_{x'y'} = \sigma_{y'x'}$ do not couple TM and TE modes.

Finally, note that, since this model is based on the semiclassical Boltzmann transport equation, it is not accurate when the spatial variations of the fields is comparable to the de Broglie wavelength of the particles [18].
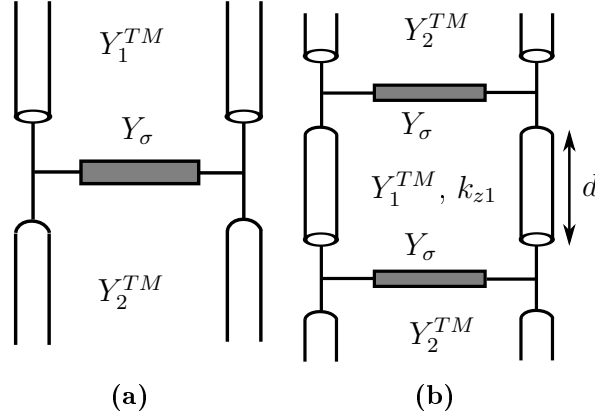
## 3.2 Single Graphene Sheet

### 3.2.1 Dispersion relation

Consider a TM surface plasmon, with frequency $\omega$ and wavevector $k_\rho$, propagating along the $+x$ direction of a graphene sheet, assuming that the sheet width is much larger than the guided wavelength, i.e. $W \gg 1/k_\rho$. This is a particular case of the strip structure considered in the lowpass filters studied in the previous chapter, where arbitrary width was allowed. This fact does not hinder the usefulness of such study, as the qualitative conclusions reached in this chapter could be applied to more complex structures, albeit without the possibility of such simple and accurate equivalent circuits.

A rigorous transverse equivalent circuit of the structure is shown in Fig. 3.2a. The equivalent admittances of the circuit are defined as

$$Y_1^{TM} = \frac{\omega\varepsilon_{r1}\varepsilon_0}{k_{z1}}, \ \ Y_2^{TM} = \frac{\omega\varepsilon_{r2}\varepsilon_0}{k_{z2}}, \ \ Y_\sigma^{TM} = \sigma(k_\rho, \omega),$$
$$k_{z1} = \pm\sqrt{\varepsilon_{r1}k_0^2 - k_\rho^2}, \ \ k_{z2} = \pm\sqrt{\varepsilon_{r2}k_0^2 - k_\rho^2}. \tag{3.9}$$

**Figure 3.2:** Transverse equivalent network of a graphene sheet (a) and a graphene-based parallel plate waveguide (b).

The dispersion relation of the plasmons propagating along the graphene sheet can be rapidly obtained by applying a transverse resonance equation [66, 67, 75] to this circuit, leading to

$$Y_1^{TM} + Y_2^{TM} = -Y_\sigma^{TM}, \tag{3.10}$$

which may be rewritten as [9]

$$\frac{\omega\varepsilon_0\varepsilon_{r1}}{\pm\sqrt{\varepsilon_{r1}k_0^2 - k_\rho^2}} + \frac{\omega\varepsilon_0\varepsilon_{r2}}{\pm\sqrt{\varepsilon_{r2}k_0^2 - k_\rho^2}} = -\sigma(k_\rho, \omega), \tag{3.11}$$

where $k_\rho = \beta - j\alpha$ is the complex propagation function of the plasmon wave, $\varepsilon_{ri}$ is the relative permittivity of the region $(i = 1, 2)$, $k_0 = \omega\sqrt{\mu_0\varepsilon_0}$ is the free-space wavenumber, and $\sigma(k_\rho, \omega)$ is the graphene's conductivity. Note that we allow accounting for potential spatial dispersion effects by explicitly writing the dependence of the conductivity with the wavevector $k_\rho$.

Let us first review, for clarity of exposition, the case of surface plasmons propagating on a laterally infinite sheet described using a local (semi-classical) graphene conductivity model. In this well-known case [9] graphene's conductivity $\sigma = \sigma_{local}$ is a frequency dependent variable that does not depend on the plasmon wavevector, defined in chapter 1, Eq. (1.1). This allows to easily obtain the propagation constant $k_\rho$ from the transcendental Eq. (3.11) using simple numerical techniques. Moreover, when the graphene sheet is embedded in a homogeneous dielectric, i.e. $\varepsilon_{r1} = \varepsilon_{r2} = \varepsilon_r$, the desired propagation constant can be obtained as

$$k_{\rho,local} = \beta_{local} - j\alpha_{local} = k\sqrt{1 - \left(\frac{2}{\eta\sigma_{local}}\right)^2}, \tag{3.12}$$

where $\eta = \sqrt{\mu_0/(\varepsilon_0 \varepsilon_r)}$ and $k = \omega\sqrt{\mu_0 \varepsilon_0 \varepsilon_r}$ are the medium impedance and wavenumber, respectively. Furthermore, in the usual non-retarded regime, i.e. when $k_\rho \gg k_0$, the plasmon wavevector can be accurately approximated as [9]

$$k_{\rho,local} \approx -j\omega\varepsilon_0 \frac{\varepsilon_{r1} + \varepsilon_{r2}}{\sigma_{local}}. \tag{3.13}$$

However, neglecting the influence of spatial dispersion may lead to significant errors when computing the properties of propagating waves at microwaves, millimeter wave and low THz frequencies. Specifically, spatial dispersion plays an important role for very slow waves ($k_\rho \gg k_0$) [69], which usually appear when graphene is surrounded by dielectrics with high-permittivity values [67].

Here, we analytically compute the dispersion relation of surface plasmon propagating along spatially dispersive graphene sheets using the conductivity model outlined earlier. Following the approach developed in [67], the dispersion relation of spatially dispersive TM surface plasmons along the $x$ axis reads

$$\frac{\omega\varepsilon_0\varepsilon_{r1}}{\sqrt{\varepsilon_{r1}k_0^2 - k_\rho^2}} + \frac{\omega\varepsilon_0\varepsilon_{r2}}{\sqrt{\varepsilon_{r2}k_0^2 - k_\rho^2}} = -\gamma\frac{\pi}{\sqrt{(\omega - j\tau^{-1})^2 - v_F^2 k_\rho^2}}, \tag{3.14}$$

where

$$\gamma = -j\frac{e^2 k_B T}{\pi^2 \hbar^2} \log\left\{2\left[1 + \cosh\left(\frac{\mu_c}{k_B T}\right)\right]\right\}. \tag{3.15}$$

Note that Eq. (3.14) is similar to the dispersion relation of surface plasmons on graphene when a local conductivity model is employed. The only difference here is the presence of the term $v_F^2 k_\rho^2$, where $v_F \approx 10^6 m/s$ is the velocity of electrons in graphene (Fermi velocity). This term explicitly indicates that the influence of spatial dispersion increases with larger wavenumbers, in agreement with the conclusions obtained using *low-$k_\rho$* approaches [67, 18].

Importantly, and in contrast to previous studies [9, 67], Eq. (3.14) admits analytical solution when the graphene sheet is surrounded by a homogeneous dielectric, i.e. $\varepsilon_{r1} = \varepsilon_{r2} = \varepsilon_r$, which is obtained as

$$k_\rho = \beta - j\alpha = k\sqrt{1 - \frac{4\varepsilon_r\left[(\omega - j\tau^{-1})^2 - k_0^2\varepsilon_r v_F^2\right]}{\eta_0^2\gamma^2\pi^2 - 4v_F^2 k_0^2\varepsilon_r^2}}. \tag{3.16}$$

Interestingly, the availability of $k_\rho$ in closed-form allows to obtain an explicit expression for the effective conductivity seen by the propagating TM surface plasmon.

This conductivity reads

$$\sigma_{xx}^{TM} = \sigma_{yy}^{TM} = \frac{1}{\eta_0}\sqrt{\frac{\pi^2\eta_0^2\gamma^2 - 4v_F^2 k_0^2 \varepsilon_r^2}{(\omega - j\tau^{-1})^2 - v_F^2 k_0^2 \varepsilon_r}}. \tag{3.17}$$

Note that this equation explicitly shows how the permittivity of the surrounding media controls the influence of spatial dispersion in graphene's conductivity.

In the non-retarded regime, the spatially dispersive plasmon wavenumber can be accurately approximated as

$$\begin{aligned}
k_\rho &\approx \frac{\omega\varepsilon_0(\varepsilon_{r1} + \varepsilon_{r2})(\omega - j\tau^{-1})}{\sqrt{\varepsilon_0^2(\varepsilon_{r1} + \varepsilon_{r2})^2 v_F^2 - \gamma^2\pi^2}} \\
&= k_{\rho,local}\frac{(\omega - j\tau^{-1})}{\sqrt{(\omega - j\tau^{-1})^2 + v_F^2 k_{\rho,local}^2}},
\end{aligned} \tag{3.18}$$

and graphene's effective TM conductivity reads

$$\sigma_{xx}^{TM} = \sigma_{yy}^{TM} = \frac{1}{\omega - j\tau^{-1}}\sqrt{\gamma^2\pi^2 - \omega^2\varepsilon_0^2(\varepsilon_{r1} + \varepsilon_{r2})^2 v_F^2}. \tag{3.19}$$

As expected, Eqs. (3.16)-(3.19) reduce to their respective well-known local expressions when spatial-dispersion effects are not considered.
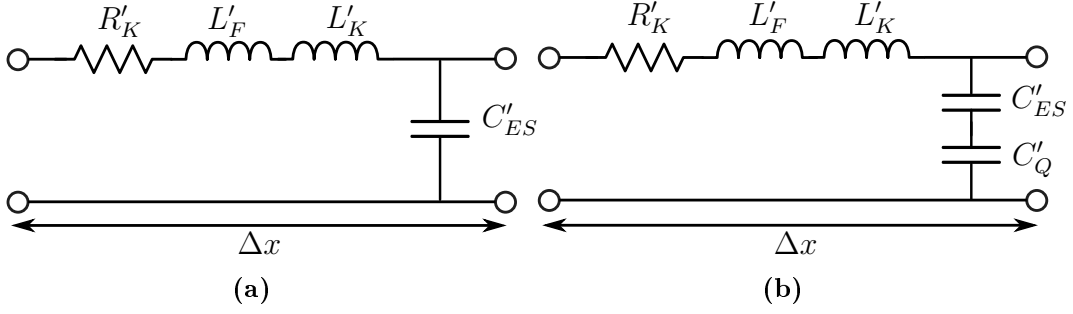
## 3.2.2   Equivalent Circuit

We will derive here rigorous per unit length equivalent circuits to characterize the longitudinal wave propagation of TM surfaces plasmon along a graphene sheet, considering both the local and non-local conductivity models.

In the local case, i.e. neglecting the presence of spatial-dispersion, this propagation can be modeled using the equivalent longitudinal circuit shown in Fig 3.3a. This circuit was recently proposed in [55] and is composed of effective TM-mode components: Faraday inductance $L_F'$, kinetic inductance $L_K'$, kinetic resistance $R_K'$ and electrostatic capacitance $C_{ES}'$. The per unit length impedance $(Z')$ and per unit length admittance $(Y')$ of the circuit are

$$Z' = R_K' + j\omega(L_F' + L_K') \;\; \text{and} \;\; Y' = j\omega C_{ES}', \tag{3.20}$$

which allows to compute the local propagation constant $k_{\rho,local}$ using standard transmission line theory [58] as

$$k_{\rho,local} = j\sqrt{Z'Y'} = \sqrt{\omega^2 C_{ES}'(L_K' + L_F') - j\omega R_K' C_{ES}'}. \tag{3.21}$$

**Figure 3.3:** Equivalent longitudinal circuit model for plasmon propagation on a graphene sheet. (a) Local model. (b) Non-local (spatially dispersive) model.

The elements of the equivalent circuit are computed using the approach detailed in [55]. This approach first derives the effective TM-mode electrostatic capacitance and Faraday inductance assuming a propagating surface plasmon with reduced attenuation factor (i.e., $\beta_{local} \gg \alpha_{local}$) by using electrostatic analysis [73], and then obtains the effective TM-mode kinetic inductance and resistance associated to the propagating wave by imposing that the circuit propagation constant must be equal to the plasmon wavenumber. Intuitively, one expects that, under certain conditions, the effective TM-mode kinetic inductance and resistance should be proportional to graphene surface impedance. Assuming that graphene is embedded within a homogeneous dielectric, the resulting expressions for the circuit elements are [55]

$$C'_{ES} = 2\varepsilon_r \varepsilon_0 \beta_{local} W, \qquad\qquad L'_F = \frac{\mu_0}{2\beta_{local} W},$$

$$L'_K = \frac{2\varepsilon_0 \varepsilon_r (\sigma_i^2 - \sigma_r^2)}{\beta_{local} W |\sigma|^4}, \qquad R'_K = \frac{4\sigma_r \sigma_i \omega \varepsilon_0 \varepsilon_r}{W \beta_{local} |\sigma|^4}. \qquad (3.22)$$

This approach is further applied here to derive the circuit elements when graphene is surrounded by different media, assuming the non-retarded regime ($k_\rho \gg k_0$). In this case, the values of the different effective TM-mode circuit elements are

$$C'_{ES} = \omega W \varepsilon_0^2 (\varepsilon_{r1} + \varepsilon_{r2})^2 \frac{\sigma_i}{\sigma_i^2 + \sigma_r^2}, \qquad L'_F = 0,$$

$$L'_K = \frac{1}{\omega W} \frac{\sigma_i^4 - \sigma_r^4}{\sigma_i |\sigma|^4}, \qquad\qquad R'_K = \frac{2}{W} \frac{\sigma_r (\sigma_i^2 + \sigma_r^2)}{|\sigma|^4}. \qquad (3.23)$$

It is important to remark that the Faraday inductance in this case is strictly zero, the electrostatic capacitance depends on the surrounding dielectric and graphene's properties, and the kinetic inductance and resistance are mainly a function of the intrinsic characteristics of graphene. The Faraday inductance arises due to the magnetic fields created around the sheet by the time-dependent oscillations of surface

33

charges. In case that $k_\rho \gg k_0$, the plasmon wavelength is very short and the charge oscillations are limited thus reducing the influence of their associated magnetic field. This behavior is explicitly shown in Eq. (3.22), where the value of the Faraday inductance is inversely proportional to the propagation phase $\beta_{local}$. Consequently, the physical assumption of the so-called non-retarded regime is to neglect the influence of the Faraday inductance.

Interestingly, in a low loss scenario ($\sigma_i \gg \sigma_r$), the lumped effective TM-mode circuit elements can be approximated as

$$R'_K \approx \frac{2}{W} R_{K_S} \quad \text{and} \quad L'_K \approx \frac{1}{W} L_{K_S}, \tag{3.24}$$

where $Z_{K_S} = 1/\sigma_{local} = R_{K_S} + j\omega L_{K_S}$ is graphene's surface impedance, where

$$L_{K_S} = \frac{1}{\omega} \frac{\sigma_i}{\sigma_i^2 + \sigma_r^2} \quad \text{and} \quad R_{K_S} = \frac{\sigma_r}{\sigma_i^2 + \sigma_r^2}, \tag{3.25}$$

with $L_{K_S} = \tau R_{K_S}$.

Eq. (3.24) explicitly shows a clear, simple, and intuitively expected relation between the equivalent circuit of TM surface plasmons and the intrinsic physical parameters of graphene.

The equations given in this Section provide simple and intuitive analytical expressions for $L'_K$ and $R'_K$ in terms of the real and imaginary parts of graphene conductivity. Specifically, the kinetic inductance $L'_K$ (associated to the inertia of carriers in alternating electric fields) is directly related to $\sigma_i$, which provides to graphene its large inductive behavior. As expected, losses contribute to reduce such effect, intuitively explaining that the real part of the conductivity results in a reduction of the kinetic inductance. In addition, the sign of $R'_K$ determines if the wave is attenuated or amplified while propagating along the sheet. In general, $\sigma_r > 0$, which leads to a positive value of $R'_K$ associated to dissipation losses. However, under population inversion conditions, negative values of $\sigma_r$ can also be obtained [29], leading to a net plasmon gain characterized by a negative resistance.

Let us focus now on the interesting case of surface plasmons propagating along a spatially dispersive laterally infinite graphene sheet. Similarly to the case of wave propagation along carbon nanotubes [74], the influence of spatial dispersion can be modeled by including an effective TM-mode quantum capacitance $C'_Q$ in series with the electrostatic capacitance (see Fig. 3.3b). This term is intrinsically related to

spatial dispersion [18] and arises due to the difference between hole and electron carrier densities in the graphene sheet [76, 77, 78]. Importantly, the local components in the circuit model (see Fig. 3.3a) remain unchanged, i.e. Eqs. (3.22)-(3.24) hold. Taking into account the presence of the quantum capacitance, the non-local propagation constant of the circuit shown in Fig. 3.3b can be obtained as

$$k_\rho = \sqrt{\omega^2 C_{total}(L'_K + L'_F) - j\omega R'_K C_{total}}, \tag{3.26}$$

where $C'^{-1}_{total} = C'^{-1}_{ES} + C'^{-1}_Q$. Following the same procedure as in the local case, i.e. imposing that this circuit propagation constant must be equal to the plasmon wavenumber [see Eq. (3.16) or Eq. (3.18)], the effective longitudinal TM-mode quantum capacitance yields

$$C'_Q = \frac{C'_{ES}(\beta^2 - \alpha^2)}{\omega^2 C'_{ES}(L'_K + L'_F) - (\beta^2 - \alpha^2)}. \tag{3.27}$$

This expression can be simplified assuming a low-loss scenario ($\sigma_i \gg \sigma_r$) and the non-retarded regime ($k_\rho \gg k_0$), by inserting Eqs. (3.18) and (3.23) into Eq. (3.27). Under these assumptions, the effective longitudinal TM-mode quantum capacitance of plasmon wave propagation can be expressed as

$$C'_{Q,approx} = \frac{W}{2} C_{Q_S}, \tag{3.28}$$

where $C_{Q_S}$ is the intrinsic quantum capacitance of graphene, which is independent of the surrounding media and is defined as [77], [78]

$$C_{Q_S} = \frac{2e^2 k_B T}{\pi \hbar^2 v_F^2} \log \left\{ 2 \left[ 1 + \cosh \left( \frac{\mu_c}{k_B T} \right) \right] \right\}. \tag{3.29}$$

The importance of the derived quantum capacitance for TM surface plasmons is twofold. First, it explicitly provides a clear and simple connection between the circuit component $C'_Q$ and the physics governing the intrinsic behavior of graphene. Second, it allows an accurate characterization of surface plasmons on spatially dispersive graphene by using a simple circuit model. Note that although the nonlocality of graphene's conductivity influences both the phase and attenuation constant of the plasmons, these variations are elegantly absorbed in the circuit by the effective TM-mode quantum capacitance, leaving the remaining components of the local circuit model unchanged.

Once analytical expressions are available for all circuit elements, additional parameters such as the characteristic impedance $Z'_C$ may be obtained using classic transmission line theory [58].

## 3.3 Graphene-based Parallel Plate Waveguides

### 3.3.1 Dispersion relation

Consider a surface wave mode propagating along the graphene-based parallel-plate waveguide illustrated in Fig. 3.1b. A rigorous transverse equivalent circuit of this structure is depicted in Fig. 3.2b, where the admittances shown in the figure are defined in Eq. (3.9). The dispersion relation of the supported plasmons can be obtained applying a transverse resonance equation to this circuit, as detailed in [68]. Employing odd and even symmetries, the dispersion relations of the modes become

$$(Y_2^{TM} + Y_\sigma^{TM}) \tan\left(k_{zs}\frac{d}{2}\right) - jY_1^{TM} = 0, \tag{3.30}$$

$$(Y_2^{TM} + Y_\sigma^{TM}) + jY_1^{TM} \tan\left(k_{z1}\frac{d}{2}\right) = 0. \tag{3.31}$$

The former mode can be seen as a perturbation of the usual TEM mode of a PPW with two perfect electric conductors [58] (odd quasi-TEM mode), whereas the latter behaves as a perturbation of the TM mode supported by a single graphene sheet [9, 68, 79] (even TM mode). Eqs. (3.30)-(3.31) do not admit analytical solutions, and purely numerical methods, such as the Newton-Raphson algorithm [80], have to be applied. Note that, in order to achieve convergence, these types of algorithms are highly dependent on the starting points employed in the complex rootsearch. Below, we provide some approximate wavenumber expressions that constitute very good starting points for this numerical search.

Let us consider first the case of surface plasmons propagating along graphene-based waveguides described using a local graphene conductivity model ($Y_\sigma^{TM} = \sigma_{local}$, see Chapter 1). The use of this model allows to obtain analytical approximate solutions for the transcendental equations shown above. Specifically, under the long wavelength approximation ($d \ll \sqrt{\varepsilon_{r1}}\lambda_0$ and $\sigma k_z/\omega\varepsilon_{r1} \gg 1$), the wavenumber of the odd quasi-TEM mode [see Eq. (3.30)] can be simplified to [68, 79]:

$$k_{\rho,local} \approx k_0\sqrt{\varepsilon_{r1}}\sqrt{1 - j\frac{2}{k_0\eta_1\sigma_{local}d}}, \tag{3.32}$$
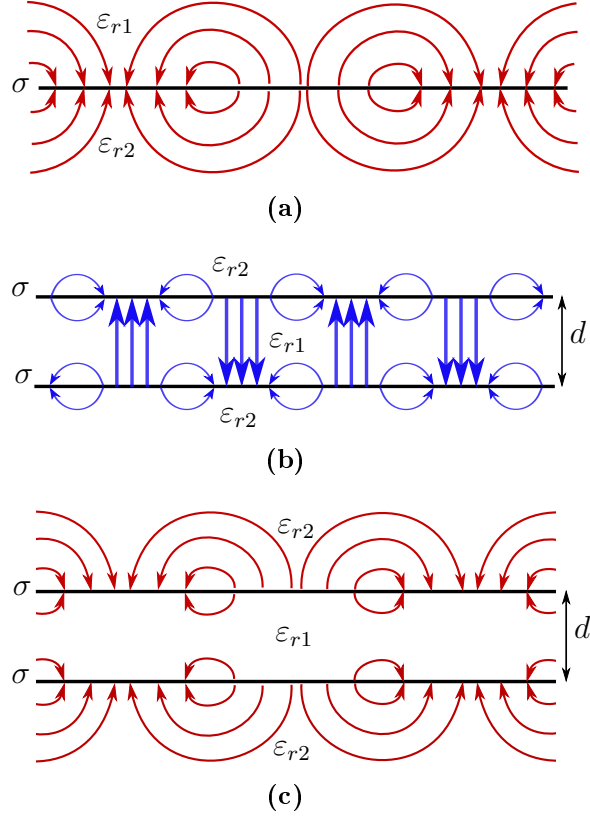
**Figure 3.4:** Electric field lines in graphene waveguides. (a) Graphene sheet TM mode. (b) Graphene parallel plate waveguide odd quasi-TEM mode. (c) Graphene parallel plate waveguide even TM mode

where $\eta_1$ is the impedance of the inner media. Note that the characteristics of this mode are mostly independent of the outer dielectric permittivity ($\varepsilon_2$), implying that the mode is highly confined between the graphene sheets (see Fig. 3.4b).

In addition, when the separation between the PPW plates is in the deep subwavelength scale ($d \ll \sqrt{\varepsilon_{r1}}\lambda_0$), the TM surface plasmons supported by each individual graphene sheet are strongly coupled, and the waveguide behaves as a single sheet with an equivalent conductivity ($\sigma_{eq}$) approximately double than that of a single graphene sheet, i.e. $\sigma_{eq} = 2\sigma_{local}$ [23]. For the transverse equivalent circuit shown in Fig. 3.2b, this approximation implies that the two graphene conductivities are in shunt, neglecting the influence of the inner dielectric. Consequently, contrary to the quasi-TEM mode, it is the outer material that mainly affects the characteristics of the TM plasmonic mode (see Fig. 3.4c). This allows to approximately solve

**(a)**
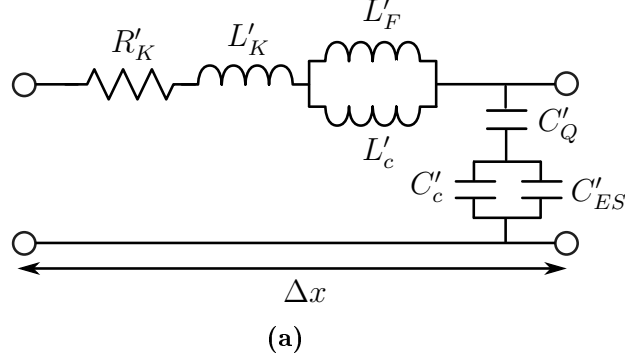
**Figure 3.5:** Equivalent longitudinal circuit model for the propagation of the quasi-TEM mode in graphene-based parallel-plate waveguides.

Eq. (3.31) as

$$k_{\rho,local} \approx \sqrt{\varepsilon_{r2}}k_0\sqrt{1 - \left(\frac{2}{\eta_2\sigma_{eq}}\right)^2},\tag{3.33}$$

where $\eta_2$ is the impedance of the outer media.

Let us now consider the influence of the spatial dispersion in the waveguides under analysis. For this purpose, the equivalent graphene admittance is set to $Y_\sigma^{TM} = \sigma_{xx} = \sigma_{yy}$, where $\sigma_{xx}$ and $\sigma_{yy}$ are defined in the previous section. Similarly to the local case, it is not possible to obtain analytical solutions to Eq. (3.30)-(3.31), and one has to resort to purely numerical methods. Importantly, the approximate wavenumbers of local [see Eq. (3.32)-(3.33)] and spatially-dispersive (see next Section) graphene-based waveguides constitute excellent initial points for the algorithm, thus allowing an efficient numerical evaluation of Eq. (3.30)-(3.31).

## 3.3.2 Equivalent Circuit

Approximate longitudinal equivalent circuits are derived to study the propagation characteristics of the quasi-TEM and TM modes supported by spatially dispersive graphene-based PPW. In both cases, the proposed circuital models are constructed based on the circuit introduced in section 3.2, which is now extended considering the physics governing each mode.

In order to derive the equivalent circuit model of the odd quasi-TEM mode, we follow the approach detailed in [73] for surface plasmons propagating along metallic PPW at optics. This approach introduces a cross-plate inductance $(L_c')$ and capacitance $(C_c')$ to characterize the interaction between the parallel plates. These

components can be obtained as [73]

$$C'_c = \varepsilon_0 \varepsilon_{r1} \frac{W}{d} e^{-\beta_{local} d}, \qquad L'_c = \mu_0 \frac{d}{W} e^{\beta_{local} d}, \qquad (3.34)$$

where $\beta_{local}$ is the phase constant of a plasmon along an isolated graphene sheet placed at the interface between media 1 and 2 [see Eq. (3.13)]. The resulting per-unit length circuit is depicted in Fig. 3.5. In addition, the intra-sheet elements are also modified to consider the coupling between the two graphene layers. Specifically, $R'_K$, $L'_K$ and $L'_F$ are multiplied by a factor of 2 to account for the series behavior of both sheets. Likewise, the intra-sheet capacitances of the graphene layers appear as reactive impedances in series, so $C'_{ES}$ and $C'_Q$ must be reduced by half [73]. The resulting circuit elements are

$$C'_{ES} = \frac{1}{2}(\varepsilon_{r1} + \varepsilon_{r2})\varepsilon_0 \beta_{local} W, \qquad L'_F = \frac{\mu_0}{\beta_{local} W},$$

$$L'_K = \frac{2}{W} L_{K_S}, \quad R'_K = \frac{4}{W} R_{K_S}, \quad C'_Q = \frac{W}{4} C_{Q_S}. \qquad (3.35)$$

The approach followed to derive the equivalent circuit of the even TM plasmonic mode is based on the approximation made in Eq. (3.33). In the conditions where Eq. (3.33) is valid, the equivalent longitudinal circuit is obtained exactly as in the case of a single sheet [see Fig. 3.3b and Eqs. (3.23)-(3.28)] which has an equivalent graphene conductivity $\sigma_{eq} = 2\sigma$ and is embedded in a material equal to the outer cladding ($\varepsilon_r = \varepsilon_{r2}$).

The limitations of the proposed equivalent circuits mainly depend on the separation distance between the graphene sheets ($d$). Importantly, both circuits provide accurate results in the deep subwavelength scale ($d \ll \sqrt{\varepsilon_1}\lambda_0$, which is the typical case of practical graphene-based PPW [81, 82]) and progressively loses accuracy as this separation increases [83]. In addition, since the quasi-TEM equivalent circuit of Fig. 3.5 takes into account the coupling between the two graphene plates [see Eq. (3.34)], it is much more robust to variations of the sheet separation distance than the TM equivalent circuit.

## 3.4   Numerical results

In this section, we first investigate the influence of spatial dispersion in the characteristics of TM surface plasmons propagating along single and parallel plate waveguides in the frequency range where intraband contributions of graphene dominate

(i.e. from microwaves to the low THz band), focusing on the impact of the surrounding media in this propagation. Furthermore, we show that the *full-$k_\rho$* conductivity model [18] employed here leads to accurate results for all surface plasmon wavenumbers, in contrast to *low-$k_\rho$* models [69] previously employed in the literature [67], [68]. Second, we demonstrate how this complex propagation phenomena can be characterized by the simple per-unit length circuital models derived in the previous sections. In addition, we analyze the behavior of the effective TM-mode circuit elements as a function of different parameters of graphene and surrounding media thus providing physical insight in the propagation of surface plasmons in graphene-based waveguides.

### 3.4.1   Single Graphene Sheet

Consider a surface plasmon propagating along a laterally infinite graphene sheet with relaxation time $\tau = 0.5$ ps and chemical potential $\mu_c = 0.05$ eV at temperature $T = 300°$ K. The characteristics of the plasmon are computed using the approach derived above and are compared to the results obtained using a *low-$k_\rho$* [67] and non spatially dispersive conductivity models. Note that using the low-$k_\rho$ conductivity model of [69] a spurious TM mode is found as an additional solution [67]. This is a non-physical mode, and has not been considered here. Moreover, the results obtained using the *full-$k_\rho$* RTA model have been further validated numerically using the Bhatnagar-Gross-Krook (BGK) conductivity model [18], confirming the accuracy of the analytical developments of Section 3.2. Figs. 3.6a-3.6b show the normalized phase ($\mathrm{Re}[k_\rho/k_0]$) and attenuation ($\mathrm{Im}[k_\rho/k_0]$) constants of the surface plasmon when graphene is standing in free-space (i.e. $\varepsilon_{r1} = \varepsilon_{r2} = \varepsilon_r = 1$). As expected [67], [69], since the propagating plasmons are not extremely slow waves ($k_\rho > k_0$), the influence of spatial dispersion is negligible in this case and the three different conductivity models provide the same results. Figs. 3.6c-3.6d present the characteristics of the surface plasmons when the graphene sheet is embedded in silicon with $\varepsilon_r = 11.9$. In this case, the presence of a dielectric with a high permittivity constant leads to very slow plasmon waves ($k_\rho \gg k_0$), a scenario in which spatial dispersion plays a significant role in determining the properties of the plasmons (see Section II and [67]). Importantly, the figures show significant differences between the results obtained using the *full-$k_\rho$* approach detailed here and the *low-$k_\rho$* method
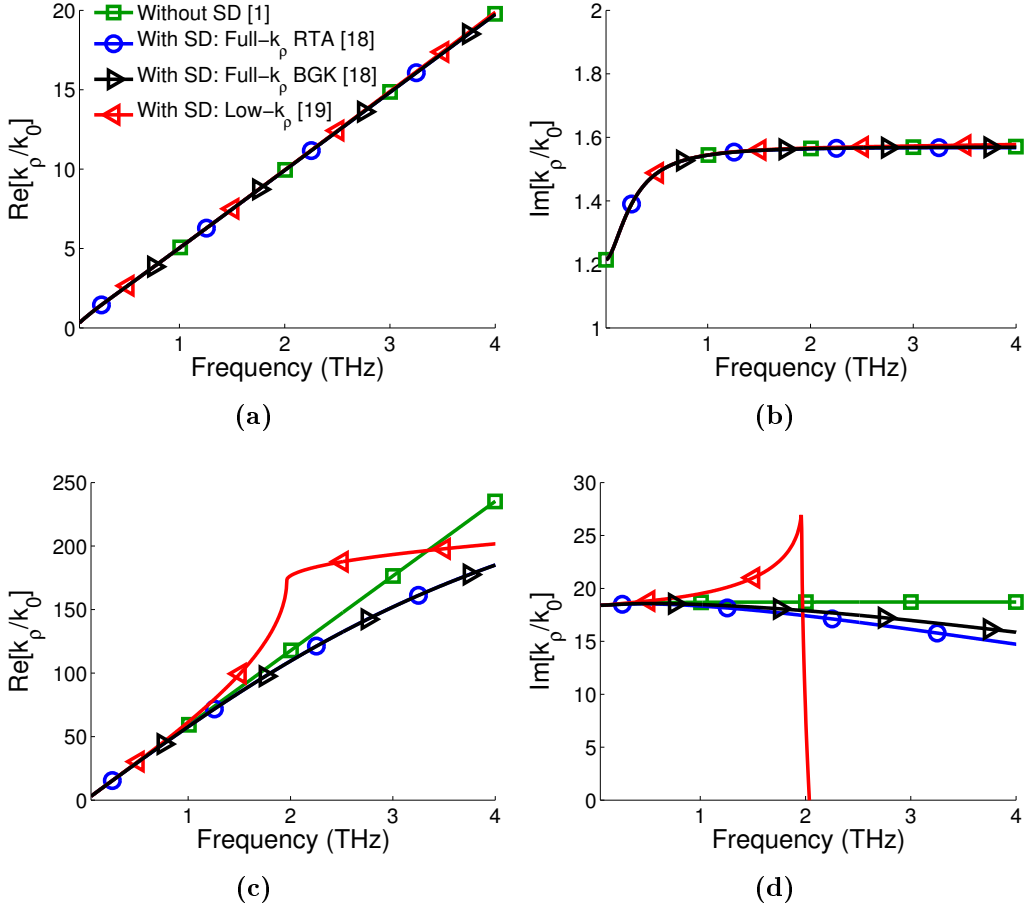
**Figure 3.6:** Characteristics of surface waves propagating along a spatially dispersive graphene sheet versus frequency . (a) and (b) show the normalized phase and attenuation constants of surface plasmons along a free-standing graphene sheet ($\varepsilon_r = 1$). (c) and (d) show the normalized phase and attenuation constants of surface plasmons along a graphene sheet embedded in silicon with $\varepsilon_r = 11.9$. Graphene parameters are $\mu_c = 0.05$ eV, $\tau = 0.5$ ps, and temperature $T = 300°$ $K$.

[67]. These differences arise because the *low-$k_\rho$* conductivity model [69] is only strictly valid for non extremely slow surface waves, specifically those which fulfill $|k_\rho| \ll \frac{|\omega - j\tau^{-1}|}{v_f}$. Note that this assumption is not fully satisfied in this particular case, and consequently, the results obtained using this approach are not accurate. On the other hand, the approach derived here is based on the *full-$k_\rho$* conductivity model [18], which does not have such limitation and is valid for any value of the plasmon wavenumber. Based on this model, results show that spatial dispersion strongly depends on the surrounding media, and that it modifies the propagating plasmons by decreasing their phase and attenuation constant.

The values of the effective TM-mode circuit model's elements able to accurately
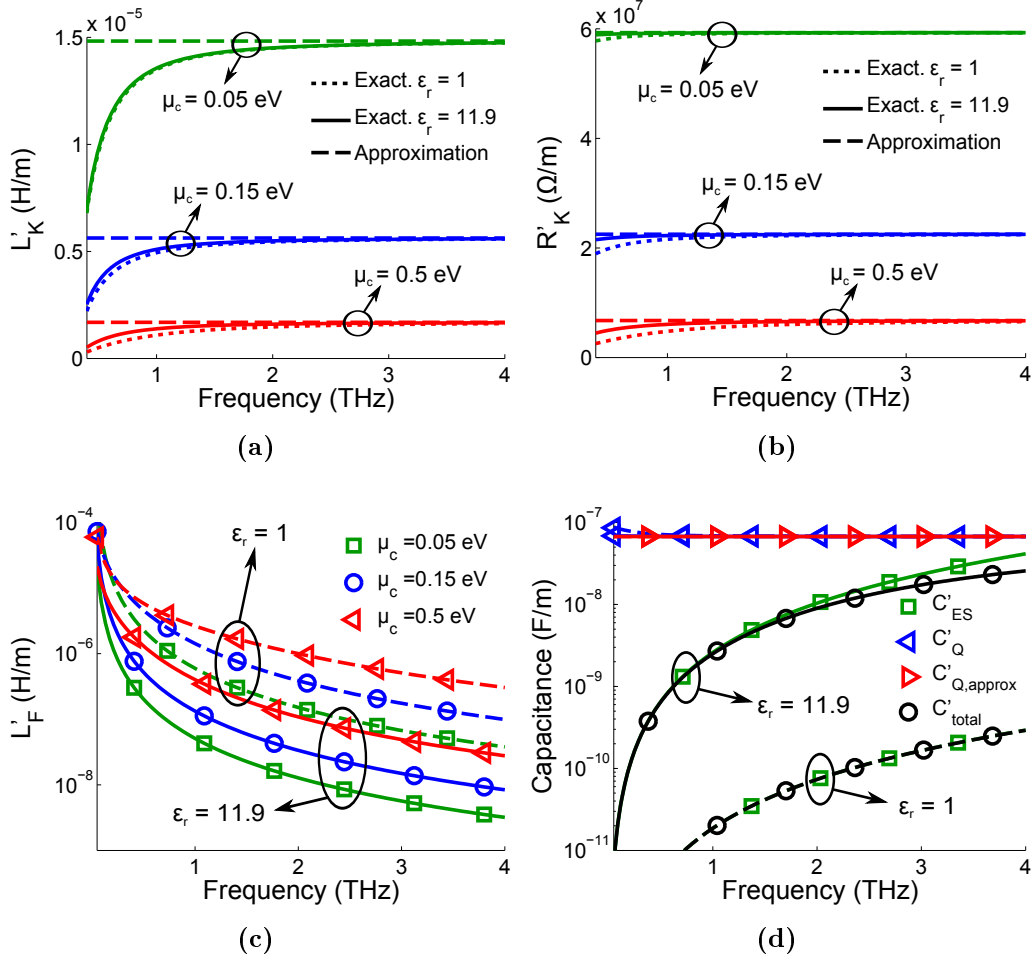
**Figure 3.7:** Study of the effective TM-mode circuit elements able to characterize surface plasmon propagation in the scenarios described in Fig. 3.6. (a) and (b) show the kinetic inductance ($L'_K$) and resistance ($R'_K$) of the circuit for different values of graphene chemical potential $\mu_c$. Results, which are independent of the surrounding media, are computed using exact [see Eq. (3.22), solid line] and approximate [see Eq. (3.24), dashed] formulas. (c) Faraday inductance $L'_F$ for various surrounding dielectric and chemical potential values. (d) Electrostatic capacitance $C'_{ES}$, exact and approximated quantum capacitances [$C'_Q$ and $C'_{Q,approx}$, related to Eq. (3.27) and Eq. (3.28), respectively] and total capacitance $C_{Q,total}$ of the circuit.

characterize plasmon propagation along spatially dispersive graphene in the two scenarios studied above are shown in Fig. 3.7. Figs. 3.7a-3.7b present the kinetic inductance and resistance of the TM surface plasmons, computed using the exact [Eq. (3.22)] and approximated [Eq. (3.24)] formulas. Results demonstrate that these elements have an almost constant behavior versus frequency, and confirm, as expected by examining Eq. (3.23) and Eq. (3.24), that the permittivity of surrounding media barely affects their value. Fig. 3.7c shows the effective TM-mode

Faraday inductance $L'_F$ of plasmons for a range of graphene chemical potentials. As expected, $L'_F$ presents values much lower than $L'_K$ in all cases, confirming that its influence is negligible in most scenarios. Fig. 3.7d depicts the effective TM-mode quantum ($C'_Q$), electrostatic ($C'_{ES}$), and total ($C'_{total}$) capacitance of the equivalent circuit. Results show that the influence of the surrounding dielectrics and frequency on the effective quantum capacitance is very limited, confirming that the expression involving the graphene intrinsic quantum capacitance [see Eq. (3.28] is an excellent approximation of the exact quantum capacitance for TM surface plasmons [see Eq. (3.27)]. However, as explicitly indicated in Eq. (3.22), these factors strongly modify the value of the electrostatic capacitance $C'_{ES}$. In the first scenario, considering a free-standing graphene sheet ($\varepsilon_r = 1$), $C'_{ES}$ is much smaller (around three orders of magnitude) than the effective quantum capacitance. Consequently, since the two capacitances are in series, $C'_{ES}$ is extremely dominant and directly provides the total capacitance $C'_{total}$ of the circuit model. This picture is completely different in the second scenario, where the presence of a dielectric with a high permittivity constant ($\varepsilon_r = 11.9$) dramatically increases the value of $C'_{ES}$. In this situation, both capacitances have values within the same order of magnitude and thus simultaneously contribute to the total capacitance of the circuit. This study provides an alternative and simple explanation to describe the influence of spatial dispersion in the characteristics of TM surface plasmons, and allows to easily identify when this phenomenon can be important by simply comparing the quantum capacitance of graphene $C'_Q$, which is an intrinsic parameter and independent of both the surrounding media and frequency, to the analytical electrostatic capacitance of the propagating plasmon.

Finally, note that the influence of spatial dispersion on the characteristics of the propagating surface plasmon mainly depends on graphene's chemical potential. Specifically, increasing the chemical potential $\mu_c$ up-shifts the frequency region where the spatial dispersion phenomenon is noticeable. Note that spatial dispersion and graphene's relaxation time are uncorrelated. These conclusions can be reached by closely examining Eq. (3.16) and Eq. (3.18), and have been confirmed by numerical simulations not shown here for the sake of compactness. Importantly, this behavior can easily be explained using the derived equivalent circuit. First, decreasing $\mu_c$ (1) increases the electrostatic capacitance, which implies that the intrinsic quantum
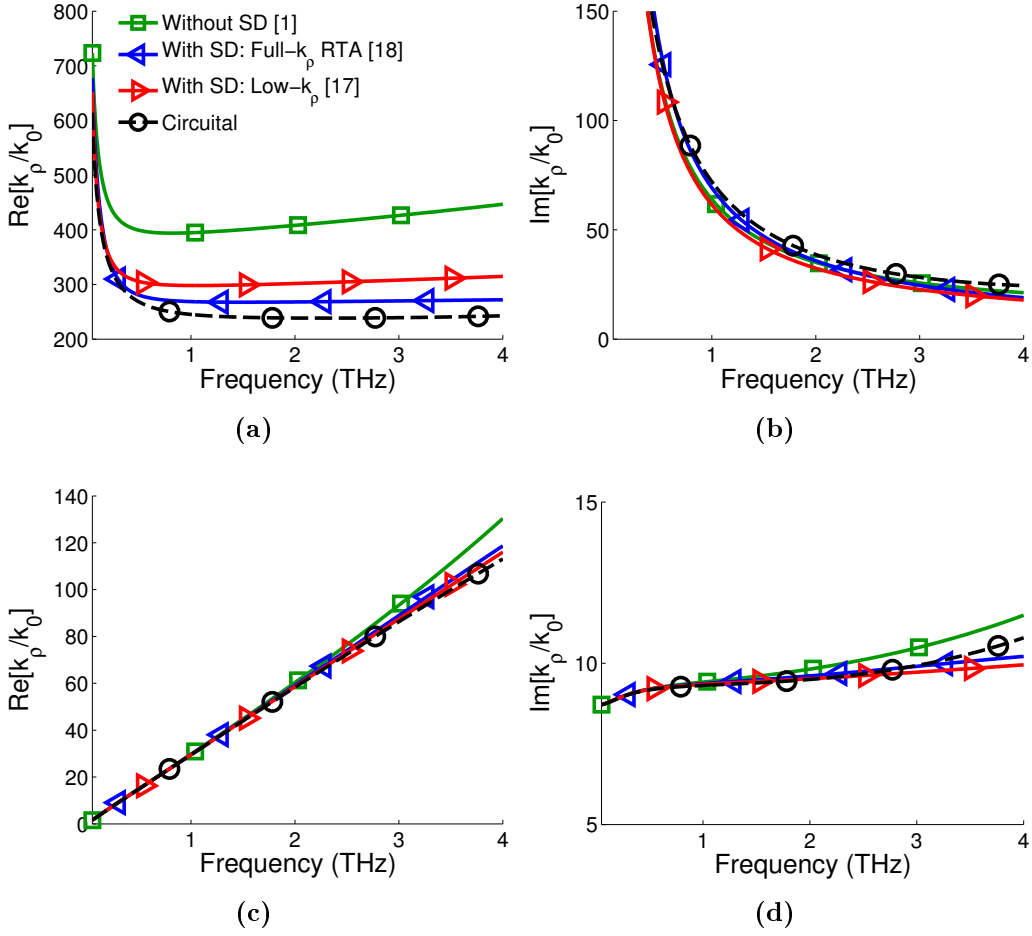
**Figure 3.8:** Characteristics of dominant modes propagating along a spatially dispersive graphene PPW versus frequency. (a) and (b) show the normalized propagation constant and losses of the quasi-TEM mode. (c) and (d) show the normalized propagation constant and losses of the TM mode. Graphene parameters are $\mu_c = 0.05$ eV, $\tau = 0.5$ ps, $\varepsilon_{r1} = \varepsilon_{r2} = 11.9$, $d = 20$ $nm$, and temperature $T = 300°$ $K$

.

capacitance cannot be neglected, and (2) increases the kinetic inductance $L'_K$ associated to the plasmon (see Fig. 3.7a) thus leading to slower surface waves. Second, the relaxation time controls the resistance $R'_K$ and the frequency range where the asymptotic approximation of $L'_K$ and $C''_Q$ are accurate but it does not modify the speed of the propagating waves, on which the influence of spatial dispersion relies.

## 3.4.2   Graphene-based Parallel Plate Waveguides

Consider a parallel-plate graphene-based waveguide with plate separation $d = 20$ nm, permittivities $\varepsilon_{r1} = \varepsilon_{r2} = 11.9$, graphene's relaxation time $\tau = 0.5$ ps and chemical potential $\mu_c = 0.05$ eV at temperature $T = 300°$ K. We have chosen this structure, composed of dielectrics with high permittivity values and sheets separation within the nanometer scale, in order to clearly identify the influence of spatial dispersion in the propagating waves. Note that very similar graphene-based PPWs have recently been fabricated, measured, and applied to modulate free-space propagating electromagnetic waves [81], [82][83]. The *full-$k_\rho$* results obtained in this Section have been computed using the RTA conductivity model. Importantly, the use of the *full-$k_\rho$* Bhatnagar-Gross-Krook (BGK) model [18] leads to extremely similar results, not shown here for the sake of clarity.

Figs. 3.8a-3.8b show the normalized phase and attenuation constants of the quasi-TEM mode. A very slow mode is found, and consequently, spatial dispersion is a dominant mechanism of wave propagation at all frequencies. Note that this phenomenon dramatically decreases the phase constant of the propagating waves, while it barely affects the losses. Moreover, the use of a *low-$k_\rho$* approximation cannot accurately model plasmon propagation in this case. The equivalent circuit model provides reasonable approximate results, with errors similar to those introduced by the *low-$k_\rho$* approach. In addition, this analytical approximation serves as an excellent starting point to solve the exact dispersion relation of Eq. (3.30) when accurate results are required. The quasi-TEM mode of a graphene-based waveguide was recently applied to design graphene phase shifters in the low THz band [32]. There, spatial dispersion was safely neglected because the waveguides were standing in free-space and the propagating plasmons were sufficiently fast. However, our results demonstrate that this mode is significantly affected by spatial dispersion, and that this phenomenon must be rigorously taken into account in the design of realistic graphene-based PPW phase-shifters and other THz components composed of dielectrics with high permittivity values.

Figs 3.8c-3.8d present the same results for the even TM mode. Despite the high permittivity of the materials composing the waveguide, this mode is found to be less sensitive to spatial dispersion than the quasi-TEM mode. Consequently, the *full-$k_\rho$*, *low-$k_\rho$*, and the circuit model lead to very similar results. This behavior is not

surprising, because this mode can be understood as a surface plasmon propagating along an equivalent graphene sheet of conductivity $\sigma_{eq} = 2\sigma$, which supports faster surface plasmons than a single graphene sheet of conductivity $\sigma$ [see Eqs. (3.12)-(3.13)].

The behavior of the different effective TM-mode circuits components and their dependence with intrinsic graphene parameters and surrounding media is similar to the case of a single graphene sheet. Regarding the cross-plate elements that appear in the odd quasi-TEM mode, it is worth mentioning that the inductive part of the circuit remains dominated by the kinetic inductance $L'_K$, whereas the cross plate capacitance $C'_c$ presents a significant contribution in most scenarios, giving to this mode its distinct dispersion curve.

## 3.5   Influence of Spatial Dispersion in Device Performance

An in depth understanding of spatial dispersion in graphene surface waves at THz frequencies has been gained from the previous section, so a natural next step in this study concerns the effect that this phenomenon may have in the performance of realistic plasmonic devices. When can the omission of spatial dispersion in the design of a device lead to significant errors? Can these errors or problems be overcome by simply performing a better optimization of the parameter space, or does spatial dispersion impose harsher limits on the achievable performance? These points will be briefly discussed in this section through the theory developed earlier and by making use of the filtering structure of chapter 2. In practice, spatial dispersion in graphene plasmonics should be accounted for if the wavenumber tangential to the graphene layer is at least two orders of magnitude larger than the free-space wavenumber ($k_{SPP} > 100k_0$), as failing to do so would induce large errors in any design.

Furthermore, high permittivity background substrates should generally be avoided in the design of graphene plasmonic components [84], since spatial dispersion imposes fundamental physical constraints on the maximum localization of SPP modes, therefore reducing the effective reconfiguration capabilities for a given range of bias voltages. This is of particular relevance in extreme subwavelength components and

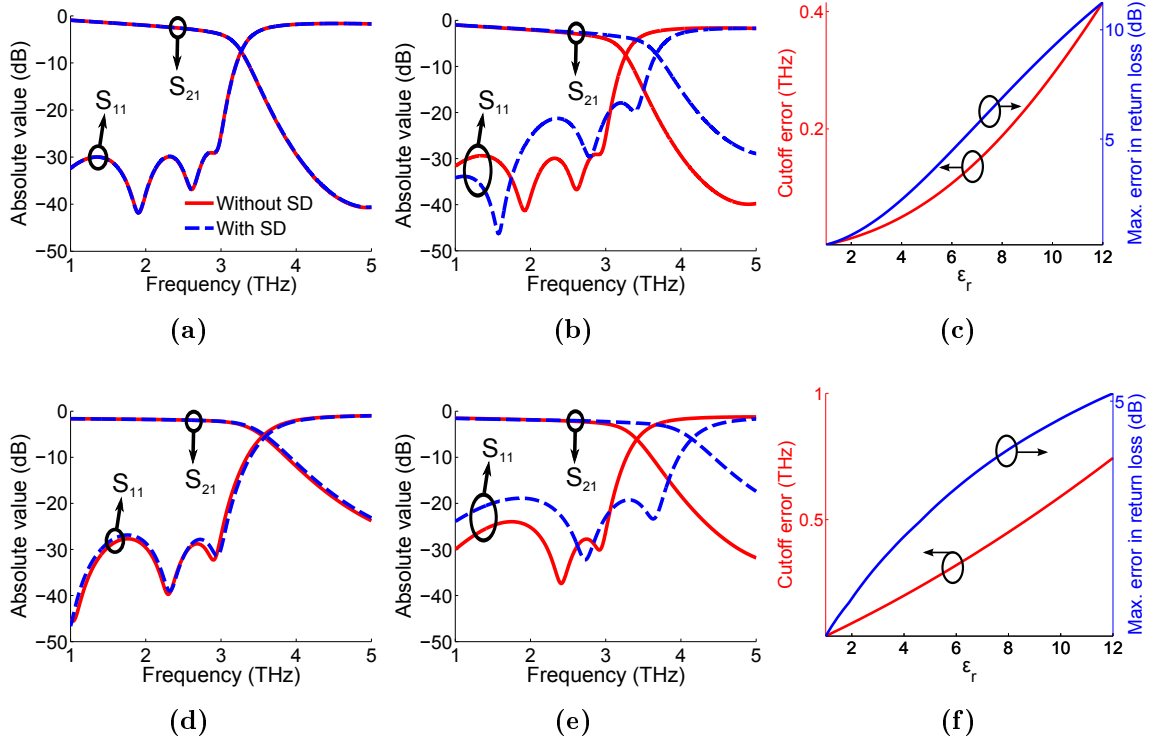**Table 3.1:** Parameters of the $7^{th}$ degree filter ($\varepsilon_r = 11.9$).

|  | $l_{sheet}(nm)$ | $\mu_{c,sheet}$ (eV) | $l_{ppw}(nm)$ | $\mu_{c,ppw}$ (eV) |
|---|---|---|---|---|
| Ports | 50 | 0.13 | 50 | 0.14 |
| 1,7 | 81 | 0.08 | 66 | 0.09 |
| 2,6 | 247 | 0.26 | 142 | 0.32 |
| 3,5 | 47 | 0.04 | 43 | 0.03 |
| 4 | 308 | 0.33 | 175 | 0.46 |

nanofocusing applications, limiting the maximum achievable enhancement of local fields.

Let us now illustrate these points by analysing realistic examples of lowpass filters like the ones designed in chapter 2, calculating the performance over a wide frequency range under the assumption of local and non-local conductivities. For convenience, we use the wide strip and parallel plate waveguides studied in this chapter as host media for these filters, and perform the analysis by combining this theory with the filter design methodology devised in Chapter 2. Specifically, we implement a $7^{th}$ degree filter with cutoff frequency $f_c = 3$ THz. For the sake of comparison, we design this filter in free-space ($\varepsilon_r = 1$) and embedded in Si ($\varepsilon_r = 11.9$). The design parameters of the Si-embedded filter, computed following chapter 2, are shown in Table 3.1. Figs. 3.9a-3.9b show the frequency response corresponding to the single graphene sheet filters, standing in free-space and embedded in Si, respectively. As expected, for $\varepsilon_r = 1$ spatial dispersion proves to be irrelevant. On the other hand, for $\varepsilon_r = 11.9$ the filter response severely deteriorates, up-shifting its cutoff frequency and unevenly increasing the reflection

throughout the passband. Note that the presence of spatial dispersion prevents the total compensation of this latter effect, due to the large frequency dispersion of the mode's propagation constant and characteristic impedance. Fig 3.9c illustrates the error in the filter's cutoff frequency and the maximum return loss in the filter's passband for various low-pass filters designed using dielectrics with increasing permittivity values. The influence of spatial dispersion increases when the permittivity of the surrounding medium increases. Figs. 3.9d-3.9f show the same study for the PPW implementation. A larger shift in the cutoff frequency is observed in this case, but interestingly, the maximum error of the return loss within the passband is lower. Contrary to the single sheet implementation, we have verified that a uniform

**Figure 3.9:** Influence of spatial dispersion in the response of $7^{th}$ degree graphene-based low-pass filters. Scattering parameters of the single sheet implementation in (a) free-space and (b) embedded in Si ($\varepsilon_{r1} = \varepsilon_{r2} = 11.9$, see Table 3.1). (c) Error in the cutoff frequency and maximum in-band reflection due to spatial dispersion as a function of surrounding permittivity. (d)-(f) show the same data for the PPW implementation (see Table 3.1). Parameters are $d = 100$ nm, $\tau = 1$ ps and $T = 300$ K (solid line - results neglecting spatial dispersion effects, dashed line - results including spatial dispersion effects)

level of in-band return loss can be achieved using graphene-based PPW, because the characteristic impedance of each spatially-dispersive transmission line section remains more linear with frequency. This indicates that the use of graphene PPW structures could be advantageous over the use of single sheet structures, when low return losses are essential in lowpass filter applications.

# Chapter 4

# Conclusions

The knowledge acquired through the development of this project is reviewed in this chapter, followed by a brief exposition of potential lines of research that naturally emerge from it.

Chapter 2 tackled the development of novel planar lowpass filters based on graphene plasmonics, for application in the THz and infrared bands. The synthesis and analysis of these filters involved the convergence of two disciplines, namely microwave filter synthesis theory and graphene plasmonics. The details regarding filter synthesis were not covered here, but are widely available in the literature. The area of graphene modelling and electromagnetic numerical simulations was covered in greater depth. In particular, we developed an efficient design technique, or scaling law, that exploits the quasi-static nature of graphene SPPs in subwavelength structures, i.e. narrow strips, to scale the numerical results of a single simulation to any point of a vast parameter space. This enables the fast synthesis of gated graphene sections with the required dimensions and characteristics that implement the transmission line segments obtained through filter synthesis theory, in a structure that would otherwise require cumbersome and slow numerical solving techniques. Several examples were studied and verified with full-wave simulations, showcasing the filtering capabilities of the proposed structure and its good performance compared to other alternatives in this frequency range, particularly in terms of miniaturization and reconfigurability. Through adequate use of electrostatic gating, the cut-off frequency of the device can be continuously tuned over a wide frequency range, resulting in a degree of tunability not achievable with any other existing technology in the THz band.

In chapter 3, the propagation of surface plasmons along spatially-dispersive graphene-based 2D waveguides was investigated in detail. Since we aimed to gain valuable physical insight and develop simple analytical tools, laterally infinite structures were considered, i.e. with a width much greater than the guided wavelength, allowing a simple analytical treatment of the problem. We used a *full-$k_\rho$* RTA conductivity formulation, which is valid up to terahertz frequencies and does not suffer from accuracy problems when dealing with extremely slow waves, as occurs with previously reported methods based on *low-$k_\rho$* approximations. The use of this model led the derivation of an analytic expression for the wavenumber of plasmons supported by spatially dispersive graphene sheets. Several per unit length equivalent circuits were introduced to accurately characterize the propagation of the different modes under study, and analytical relations between the effective TM-mode circuit lumped elements and the intrinsic properties of graphene were derived. Importantly, an effective TM-mode quantum capacitance lumped component accurately models the spatial dispersion phenomenon in all equivalent circuits. Results obtained with the derived equivalent circuits are in good agreement with the rigorous solutions obtained from solving exact transverse resonance equations, thus validating the theory proposed. The chapter demonstrated that spatial dispersion significantly decreases the confinement and the losses of slow surface plasmons when dielectrics of high permittivity values are used as supporting material. This indicates that spatial dispersion must be rigorously taken into account when designing graphene-based plasmonic components at millimeter-waves and low terahertz frequencies. To evaluate this findings in more practical scenarios, we studied the influence of non-local effects in the response and performance of the filters developed in the second chapter, using now the spatially dispersive waveguides of chapter 3 as host medium. Due to the extremely slow waves supported by graphene-based waveguides in the presence of high permittivity media, it was clearly illustrated that spatial dispersion becomes a significant mechanism of propagation that modifies the expected behavior of these devices by up-shifting their operation frequency, limiting their tunable range, and degrading their frequency response. Consequently, spatial dispersion must be accurately taken into account in the development of graphene-based plasmonic THz devices.

The work done in this project may serve as the foundation of future research in

the field of graphene filter design. Several aspects are open to further optimization, and the possibility of synthesizing different transfer functions and using alternate physical implementations is an exciting topic. A prototype network based on normalized transmission lines and impedance inverters could be used for the design of the lowpass filter functions, instead of the one employed here. Appropriate design of the impedance inverters would minimize the degradation of performance cause by the soft boundary conditions created by the fringing electrostatic fields between adjacent gates. This is analogous to what occurs in microwave waveguide filters, where impedance inverters are designed to include the effects of non-ideal irises, so that the prototype network may be more accurately implemented. There also exists the possibility of using more complex patterns or combining graphene with other technologies such as metasurfaces to reduce losses or increase the spurious-free range. The design of bandpass filters through similar methods could also be explored. This presents additional challenges, as the additional electrical length required to implement resonators will inevitably increase the insertion loss of the device. Regarding spatial dispersion effects, in order to fully grasp the potential of graphene nanoplasmonics, it is of great importance to further explore the limits that fundamental physics impose on the maximum confinement and field enhancement achievable. Such understanding will be necessary in future highly miniaturized plasmonic systems and nanofocusing applications.

We hope the findings and design techniques presented in this work may serve scientists and engineers interested in these topics, and those who work in related fields, as a foundation for exciting advances in THz technology.

# Appendix A

# Author's Publications

## A.1 International Refereed Journals

J1 **D. Correas-Serrano**, J. S. Gómez-Díaz, A. Alù and A. Álvarez Melcón, "Electrically and Magnetically Biased Graphene-based Cylindrical Waveguides: Analysis and Applications as Reconfigurable Antennas", IEEE Trans. Terahertz Science and Technology, [Under review. Current status: Accepted subject to minor changes].

J2 **D. Correas-Serrano**, J. S. Gómez-Díaz, J. Perruisseau-Carrier and A. Alvarez-Melcón, "Graphene based plasmonic tunable low pass filters in the THz band", *IEEE Transactions on Nanotechnology, IEEE Trans. Nanotechnology*, vol. 13, no. 6, pp. 1145-1153, Nov 2014.

J3 P. Vera-Castejon, **D. Correas-Serrano**, F. Quesada-Pereira, J. Hinojosa and A. Alvarez-Melcón, "A Novel Low-Pass Filter Based on Circular Posts Designed by an Alternative Full-Wave Analysis Technique," *IEEE Trans. Microwave Theory and Techniques*, vol. 62, pp 2300-2307, 2014.

J4 **D. Correas-Serrano**, J. S. Gómez-Díaz and A. Alvarez-Melcón, "On the Influence of Spatial Dispersion on the Performance of Graphene-Based Plasmonic Devices," *IEEE Antennas and Wireless Propagation Letters*, vol. 13, pp.345-348, 2014.

J5 **D. Correas-Serrano**, J. S. Gómez-Díaz, J. Perruisseau-Carrier and A. Alvarez-Melcón, "Spatially Dispersive Graphene Single and Parallel Plate Waveguides:

Analysis and Circuit Model," *IEEE Transactions of Microwave Theory and Techniques*, vol. 61, pp. 4333-4344, 2013.

## A.2    International Conference Proceedings

C1 **D. Correas-Serrano**, J. S. Gómez-Díaz, A. Alvarez-Melcón and A. Alù, "Surface Plasmon Modes in Self-Biased Coupled Graphene-Coated Wires," *International Symposium on Antennas and Propagation, 2015.*

C2 **D. Correas-Serrano**, J. S. Gómez-Díaz and A. Alvarez-Melcón, "Plasmonic Devices and Spatial Dispersion Effects in Graphene Technology for Terahertz Applications," *International Symposium on Antennas and Propagation, 2015.*

C3 **D. Correas-Serrano**, J. S. Gómez-Díaz and A. Alvarez-Melcón, "Surface Plasmons in Graphene Cylindrical Waveguides," *International Symposium on Antennas and Propagation, 2014.*

C4 **D. Correas-Serrano**, J. S. Gómez-Díaz ,J. Perruisseau-Carrier and A. Alvarez-Melcón, "Study of Spatial Dispersion in Graphene Parallel-Plate Waveguides and Equivalent Circuit," *European Conference on Antennas and Propagation (EuCAP), 2014.*

# Bibliography

[1] Masayoshi Tonouchi. Cutting-edge terahertz technology. *Nature photonics*, 1(2):97–105, 2007.

[2] Bradley Ferguson and Xi-Cheng Zhang. Materials for terahertz science and technology. *Nature materials*, 1(1):26–33, 2002.

[3] Tony Low and Phaedon Avouris. Graphene plasmonics for terahertz to mid-infrared applications. *Acs Nano*, 8(2):1086–1101, 2014.

[4] JB Pendry, L Martin-Moreno, and FJ Garcia-Vidal. Mimicking surface plasmons with structured surfaces. *Science*, 305(5685):847–848, 2004.

[5] Anders Pors, Esteban Moreno, Luis Martin-Moreno, John B Pendry, and Francisco J Garcia-Vidal. Localized spoof plasmons arise while texturing closed surfaces. *Physical review letters*, 108(22):223905, 2012.

[6] Hugen Yan, Xuesong Li, Bhupesh Chandra, George Tulevski, Yanqing Wu, Marcus Freitag, Wenjuan Zhu, Phaedon Avouris, and Fengnian Xia. Tunable infrared plasmonic devices using graphene/insulator stacks. *Nature Nanotechnology*, 7(5):330–334, 2012.

[7] Hugen Yan, Tony Low, Wenjuan Zhu, Yanqing Wu, Marcus Freitag, Xuesong Li, Francisco Guinea, Phaedon Avouris, and Fengnian Xia. Damping pathways of mid-infrared plasmons in graphene nanostructures. *Nature Photonics*, 7(5):394–399, 2013.

[8] Long Ju, Baisong Geng, Jason Horng, Caglar Girit, Michael Martin, Zhao Hao, Hans A Bechtel, Xiaogan Liang, Alex Zettl, Y Ron Shen, et al. Graphene plas-

56

monics for tunable terahertz metamaterials. *Nature nanotechnology*, 6(10):630–634, 2011.

[9] M. Jablan, H. Buljan, and M. Soljacic. Plasmonics in graphene at infrared frequencies. *Physical review B*, 80:245435, 2009.

[10] J. Chen, M. Badioli, P. Alonso-Gonzalez, S. Thongrattanasiri, F. Huth, J. Osmond, M. Spasenovic, A. Centeno, A. Pesquera, P. Godignon, A. Zurutuza-Elorza, N. Camara, F. J. Garcia de Abajo, R. Hillenbrand, and F. H. L. Koppens. Optical nano-imaging of gate-tunable graphene plasmons. *Nature*, 487:77–81, 2012.

[11] A. H. Castro Neto, N. M. R. Peres, K. S. Novoselov, and A. K. Geim. The electronic properties of graphene. *Reviews of Modern Physics*, 81:109–162, January 2009.

[12] K. S. Novoselov, A. K. Geim, S. V. Morozov, D. Jiang, Y. Zhang, S. .V. Dubonos, I. V. Grigorieva, and A. A. Firsov. Electric field effect in atomically thin carbo filts. *Science*, 306:666–669, 2004.

[13] A. Vakil and N. Engheta. Transformation optics using graphene. *Science*, 332:1291–1294, 2011.

[14] EH Hwang and S Das Sarma. Acoustic phonon scattering limited carrier mobility in two-dimensional extrinsic graphene. *Physical Review B*, 77(11):115449, 2008.

[15] J. S. Gomez-Diaz and J. Perruisseau-Carrier. Propagation of hybrid transverse magnetic-transverse electric plasmons on magnetically-biased graphene sheets. *Journal of Applied Physics*, 112:124906, 2012.

[16] G. W. Hanson. Dyadic green's functions and guided surface waves for a surface conductivity of graphene. *Journal of Applied Physics*, 103:064302, 2008.

[17] V. P. Gusynin, S. G. Sharapov, and J. B. Carbotte. On the universal ac optical background in graphene. *New J. Physics*, 11:095013, 2009.

[18] G. Lovat, G. W. Hanson, R. Araneo, and P. Burghignoli. Semiclassical spatially dispersive intraband conductivity tensor and quantum capacitance of graphene. *Physical Review B*, 87:115429, 2013.

[19] Tsuneya Ando. The electronic properties of graphene and carbon nanotubes. *NPG Asia Materials*, 1(1):17–21, 2009.

[20] Jason Horng, Chi-Fan Chen, Baisong Geng, Caglar Girit, Yuanbo Zhang, Zhao Hao, Hans A Bechtel, Michael Martin, Alex Zettl, Michael F Crommie, et al. Drude conductivity of dirac fermions in graphene. *Physical Review B*, 83(16):165113, 2011.

[21] A. Yu. Nikitin, F. Guinea, F. J. García-Vidal, and L Martín-Moreno. Edge and waveguide terahertz surface plasmon modes in graphene microribbons. *Phys. Rev. B*, 84:161407, 2011.

[22] J. Christensen, A. Manjavacas, S. Thongrattanasiri, F. H. L. Koppens, and F. J. García de Abajo. Graphene plasmon waveguiding and hybridization in individual and paired nanoribbons. *ACS Nano*, 6:431–440, 2012.

[23] M. Tamagnone, J. S. Gomez-Díaz, J. R. Mosig, and J. Perruisseau-Carrier. Reconfigurable thz plasmonic antenna concept using a graphene stack. *Applied Physics Letters*, 101:214102, 2012.

[24] R. Filter, M. Farhat, M. Steglich, R. Alaee, C. Rockstuhl, and F. Lederer. Tunable graphene antennas for selective enhancement of thz-emission. *Optics Express*, 21:3737–3745, 2013.

[25] Yi Huang, Lin-Sheng Wu, Min Tang, and Junfa Mao. Design of a beam reconfigurable thz antenna with graphene-based switchable high-impedance surface. *Nanotechnology, IEEE Transactions on*, 11(4):836–842, 2012.

[26] Marc Esquius-Morote, JS Gomez-Diaz, and Julien Perruisseau-Carrier. Sinusoidally modulated graphene leaky-wave antenna for electronic beamscanning at thz. *Terahertz Science and Technology, IEEE Transactions on*, 4(1):116–122, 2014.

[27] JS Gomez-Diaz, M Esquius-Morote, and J Perruisseau-Carrier. Plane wave excitation-detection of non-resonant plasmons along finite-width graphene strips. *Optics Express*, 21(21):24856–24872, 2013.

[28] E. Carrasco and J. Perruisseau-Carrier. Tunable graphene reflective cells for thz reflectarrays and generalized law of reflection. *Applied Physics Letters*, 102:104103, 2013.

[29] F. Rana. Graphene terahertz plasmon oscillators. *IEEE Trans. Nanotech.*, 7:91–99, 2008.

[30] Juan-Sebastian Gomez-Diaz and Julien Perruisseau-Carrier. Graphene-based plasmonic switches at near infrared frequencies. *Optics Express*, 21(13):15490–15504, 2013.

[31] B. Sensale-Rodriguez, R. Yan, M. M. Kelly, T. Fang, K. Tahy, W. S. Hwang, D. Jena, L. Liu, and H. G. Xing. Broadband graphene terahertz modulators enabled by intraband transitions. *Nature Communications*, 3:780, 2012.

[32] P. Y. Chen, C. Argyropoulos, and A. Alu. Terahertz antenna phase shifters using integrally-gated graphene transmission-lines. *IEEE Transactions on Antennas and Propagation*, 61:1528 – 1537, 2013.

[33] R. Arsat, M. Breedon, M. Shafiei, P. G. Spizziri, S. Gilje, R. B. Kaner, K. Kalantar-zadeh, and W. Wlodarski. Graphene-like nano-sheets for surface acoustic wave gas sensor applications. *Chemical Physics Letters*, 467:344–347, 2009.

[34] X. Kang, J. Wang, H. Wu, J. Lui, I. A. Aksay, and Y. Lin. A graphene-based electrochemical sensor for sensitive detection of paracetamol. *Talanta*, 81:754–759, 2010.

[35] John F Federici, Brian Schulkin, Feng Huang, Dale Gary, Robert Barat, Filipe Oliveira, and David Zimdars. Thz imaging and sensing for security applications: explosives, weapons and drugs. *Semiconductor Science and Technology*, 20(7):S266, 2005.

[36] Antoni Rogalski. Infrared detectors: status and trends. *Progress in quantum electronics*, 27(2):59–210, 2003.

[37] V.M. Lubecke, Koji Mizuno, and G.M. Rebeiz. Micromachining for terahertz applications. *Microwave Theory and Techniques, IEEE Transactions on*, 46(11):1821–1831, 1998.

[38] William F Andress, Hosang Yoon, Kitty YM Yeung, Ling Qin, Ken West, Loren Pfeiffer, and Donhee Ham. Ultra-subwavelength two-dimensional plasmonic circuits. *Nano letters*, 12(5):2272–2277, 2012.

[39] F. Schuster, D. Coquillat, H. Videlier, M. Sakowicz, and F. Teppe et al. Broadband terahertz imaging with highly sensitive silicon cmos detectors. *Optics Express*, 19(8):7827–7832, 2011.

[40] S. Boppel, A. Lisauskas, V. Krozer, and H.G. Roskos. Performance and performance variations of sub-1 thz detectors fabricated with 0.15 $\mu m$ cmos foundry process. *Electronics Letters*, 47(11):661–662, 2011.

[41] Eui Su Lee, Sun-Goo Lee, Chul-Sik Kee, and Tae-In Jeon. Terahertz notch and low-pass filters based on band gaps properties by using metal slits in tapered parallel-plate waveguides. *Optics Express*, 19(16):14852–14859, 2011.

[42] Dongmin Wu, Nicholas Fang, Cheng Sun, Xiang Zhang, Willie J Padilla, Dimitri N Basov, David R Smith, and Sheldon Schultz. Terahertz plasmonic high pass filter. *Applied Physics Letters*, 83(1):201–203, 2003.

[43] Mingzhi Lu, Wenzao Li, and Elliott R Brown. Second-order bandpass terahertz filter achieved by multilayer complementary metamaterial structures. *Optics letters*, 36(7):1071–1073, 2011.

[44] J Cunningham, C Wood, AG Davies, I Hunter, EH Linfield, and HE Beere. Terahertz frequency range band-stop filters. *Applied Physics Letters*, 86(21):213503–213503, 2005.

[45] Xian-Shi Lin and Xu-Guang Huang. Tooth-shaped plasmonic waveguide filters with nanometeric sizes. *Optic Letters*, 33(23), 2008.

[46] J. H. Zhu, Qi J. Wang, P. Shum, and Xu G. Huang. A nanoplasmonic high-pass wavelength filter based on a metal-insulator-metal circuitous waveguide. *IEEE Transactions on Nanotechnology*, 10(6), 2011.

[47] Binfeng Yun, Guohua Hu, and Yiping Cui. Theoretical analysis of a nanoscale plasmonic filter based on a rectangular metal–insulator–metal waveguide. *Journal of Physics D: Applied Physics*, 43(38):385102, 2010.

[48] F Javier Garcia de Abajo. Multiple excitation of confined graphene plasmons by single free electrons. *ACS nano*, 7(12):11409–11419, 2013.

[49] Jianing Chen, Michela Badioli, Pablo Alonso-Gonzalez, Sukosin Thongrattanasiri, Florian Huth, Johann Osmond, Marko Spasenović, Alba Centeno, Amaia Pesquera, Philippe Godignon, et al. Optical nano-imaging of gate-tunable graphene plasmons. *Nature*, 2012.

[50] Andreas Otto. Excitation of nonradiative surface plasma waves in silver by the method of frustrated total reflection. *Zeitschrift für Physik*, 216(4):398–410, 1968.

[51] Weilu Gao, Jie Shu, Ciyuan Qiu, and Qianfan Xu. Excitation of plasmonic waves in graphene by guided-mode resonances. *ACS nano*, 6(9):7806–7813, 2012.

[52] NMR Peres, Yu V Bludov, Aires Ferreira, and MI Vasilevskiy. Exact solution for square-wave grating covered with graphene: surface plasmon-polaritons in the terahertz range. *Journal of Physics: Condensed Matter*, 25(12):125303, 2013.

[53] Yu V Bludov, Aires Ferreira, NMR Peres, and MI Vasilevskiy. A primer on surface plasmon-polaritons in graphene. *International Journal of Modern Physics B*, 27(10), 2013.

[54] Arthur R Davoyan, Vyacheslav V Popov, and Sergei A Nikitov. Tailoring terahertz near-field enhancement via two-dimensional plasmons. *Physical Review Letters*, 108(12):127401, 2012.

[55] J. S. Gomez-Diaz and J. Perruisseau-Carrier. A transmission line model for plasmon propagation on a graphene strip. In *IEEE International Microwave Symposium*, Seattle, USA, 2013.

[56] Gregory R Aizin and Gregory C Dyer. Transmission line theory of collective plasma excitations in periodic two-dimensional electron systems: Finite plasmonic crystals and tamm states. *Physical Review B*, 86(23):235316, 2012.

[57] R. J. Cameron, R. Mansour, and C. M. Kudsia. *Microwave Filters for Communication Systems: Fundamentals, Design and Applications*. Wiley-Blackwell, 2007.

[58] D. Pozar. *Microwave Engineering*. John Wiley and Sons, 3$^{\text{rd}}$ edition, 2005.

[59] D. Correas-Serrano, J. S. Gomez-Diaz, J. Perruisseau-Carrier, and A. Alvarez-Melcon. Spatially dispersive graphene single and parallel plate waveguides: analysis and circuit model. *IEEE Transactions on Microwave Theory and Techniques*, 61(12):4333 – 4344, December 2013.

[60] Z. Fang, S. Thongrattanasiri, A. Schlather, Z. Liu, and L. Ma et al. Gated tunability and hybridization of localized plasmons in nanostructured graphene. *ACS Nano*, 7:2388Ũ2395, 2013.

[61] L. Fan, M. Y. Li, and K. Chang. Circular waveguide to microstrip transitions. *Electronics Letters*, 31(4):294–295, February 1995.

[62] Ebrahim Forati and George W Hanson. Soft-boundary graphene nanoribbon formed by a graphene sheet above a perturbed ground plane: conductivity profile and spp modal current distribution. *Journal of Optics*, 15(11):114006, 2013.

[63] RJ Pryputniewicz. Mems summitv technology. *Worcester Polytechnic Institute, Worcester MA*, 2002.

[64] CR Dean, AF Young, I Meric, C Lee, L Wang, S Sorgenfrei, K Watanabe, T Taniguchi, P Kim, KL Shepard, et al. Boron nitride substrates for high-quality graphene electronics. *Nature nanotechnology*, 5(10):722–726, 2010.

[65] A. Ferreira, N. M. R. Peres, and A. H. Castro Neto. Confined magneto-optical waves in graphene. *Physical Review B*, 85:205426, 2012.

[66] G. Lovat. Equivalent circuit for electromagnetic interaction and transmission through graphene sheets. *IEEE Transactions on Electromagnetic Compatibility*, 54:101–109, February 2012.

[67] J. S. Gomez-Diaz, J. R. Mosig, and J. Perruisseau-Carrier. Effect of spatial dispersion on surfaces waves propagating along graphene sheets. *IEEE Transactions on Antennas and Propagation*, 61:3589–3596, 2013.

[68] G. Lovat, P. Burghignoli, and R. Araneo. Low-frequency dominant-mode propagation in spatially dispersive graphene nanowaveguides. *IEEE Transactions on Electromagnetic Compatibility*, 11:1489–1492, 2013.

[69] G. W. Hanson. Dyadic green's functions for an anisotropic non-local model of biased graphene. *IEEE Transactions on Antennas and Propagation*, 56(3):747–757, March 2008.

[70] G. W. Hanson, A. B. Yakovlev, and A. Mafi. Excitation of discrete and continuous spectrum for a surface conductivity model of graphene. *Journal of Applied Physics*, 110:114305, January 2011.

[71] Frank HL Koppens, Darrick E Chang, and F Javier Garcia de Abajo. Graphene plasmonics: a platform for strong light–matter interactions. *Nano letters*, 11(8):3370–3377, 2011.

[72] Jianing Chen, Michela Badioli, Pablo Alonso-González, Sukosin Thongrattanasiri, Florian Huth, Johann Osmond, Marko Spasenović, Alba Centeno, Amaia Pesquera, Philippe Godignon, et al. Optical nano-imaging of gate-tunable graphene plasmons. *Nature*, 2012.

[73] M. Staffaroni, J. Conway, S. Vedantam, J. Tang, and E. Yablonovitch. Circuit analysis in metal-optics. *Photonics and Nanostructures - Fundamentals and Applications*, 10:166–176, 2012.

[74] P. J. Burke. An RF circuit model for carbon nanotubes. *IEEE Transactions on Nanotechnology*, 2:55–58, 2002.

[75] R. E. Collin and F. J. Zucker. *Antenna Theory.* McGraw-Hill, 1969.

[76] Z. Chen and J. Appenzeller. Mobility extraction and quantum capacitance impact in high performance graphene field-effect transistor devices. In *IEEE International Electron Devices Meeting (IEDM)*, San Francisco, USA, 15-17 Dec. 2008.

[77] T. Fang, A. Konar, H. Xing, and D. Jena. Carrier statistics and quantum capacitance of graphene sheets and rib. *Applied Physics Letters*, 91:092109, 2007.

[78] Jilin Xia, Fang Chen, Jinghong Li, and Nongjian Tao. Measurement of the quantum capacitance of graphene. *Nature nanotechnology*, 4(8):505–509, 2009.

[79] G. W. Hanson. Quasi-transverse electromagnetic modes supported by a graphene parallel-plate waveguide. *Journal of Applied Physics*, 104:084314, 2008.

[80] W. H. Press, S. A. Teukolsky, W. T. Vetterling, and B. P. Flannery. *Numerical Recipes in Fortran 77, The Art of Scientific Computing.* Cambridge University Press, 1996.

[81] M. Liu, X. Yin, E. U. Avila, B. Geng, T. Zentgraf, L.Ju, F. Wang, and X. Zhang. A graphene-based broadband optical modulator. *Nature Letters*, 474:64Ű67, 2011.

[82] M. Liu, X. Yin, and X. Zhang. Double-layer graphene optical modulator. *Nano Letters*, 12(3):1482Ű1485, 2012.

[83] JS Gomez-Diaz, C Moldovan, S Capdevilla, J Romeu, LS Bernard, A Magrez, AM Ionescu, and J Perruisseau-Carrier. Self-biased reconfigurable graphene stacks for terahertz plasmonics. *Nature Communications*, 6:6334, 2015.

[84] D. Correas-Serrano, J.S. Gomez-Diaz, and A. Alvarez-Melcon. On the influence of spatial dispersion on the performance of graphene-based plasmonic devices. *Antennas and Wireless Propagation Letters, IEEE*, 13:345–348, 2014.